Monthly Notices of the ROYAL ASTRONOMICAL SOCIETY

MNRAS **529,** 3630–3650 (2024) https://doi.org/10.1093/mnras/stae738
Advance Access publication 2024 March 15

Red supergiant candidates for multimessenger monitoring of the next Galactic supernova

Sarah Healy [1★] Shunsaku Horiuchi [1,2] Marta Colomer Molla,[3] Dan Milisavljevic,[4,5] Jeff Tseng,[6] Faith Bergin,[4] Kathryn Weil [4] Masaomi Tanaka [7] and Sebastián Otero[8]

[1]*Center for Neutrino Physics, Department of Physics, Virginia Tech, Blacksburg, VA 24061, USA*
[2]*Kavli IPMU (WPI), UTIAS, The University of Tokyo, Kashiwa, Chiba 277-8583, Japan*
[3]*Université Libre de Bruxelles, 1050 Bruxelles, Belgium*
[4]*Department of Physics and Astronomy, Purdue University, West Lafayette, IN 47907, USA*
[5]*Integrative Data Science Initiative, Purdue University, West Lafayette, IN 47907, USA*
[6]*Department of Physics, Oxford University, Oxford OX1 3RH, UK*
[7]*Astronomical Institute, Tohoku University, Sendai 980-8578, Japan*
[8]*American Association of Variable Star Observers (AAVSO), Cambridge, MA 02138, USA*

Accepted 2024 March 7. Received 2024 March 6; in original form 2023 July 28

ABSTRACT

We compile a catalogue of 578 highly probable and 62 likely red supergiants (RSGs) of the Milky Way, which represents the largest list of Galactic RSG candidates designed for continuous follow-up efforts to date. We match distances measured by *Gaia* DR3, 2MASS photometry, and a 3D Galactic dust map to obtain luminous bright late-type stars. Determining the stars' bolometric luminosities and effective temperatures, we compare to Geneva stellar evolution tracks to determine likely RSG candidates, and quantify contamination using a catalogue of Galactic AGB in the same luminosity-temperature space. We add details for common or interesting characteristics of RSG, such as multistar system membership, variability, and classification as a runaway. As potential future core-collapse supernova progenitors, we study the ability of the catalogue to inform the Supernova Early Warning System (SNEWS) coincidence network made to automate pointing, and show that for 3D position estimates made possible by neutrinos, the number of progenitor candidates can be significantly reduced, improving our ability to observe the progenitor pre-explosion and the early phases of core-collapse supernovae.

Key words: astroparticle physics – catalogues – stars: late-type – (stars:) supergiants – transients: supernovae.

1 INTRODUCTION

Red Supergiants (RSGs) are one of the last evolutionary stages of massive stars, and have been directly linked to Type-IIP/L supernovae (SNe) through matching SN locations with archival pre-explosion images (Smartt et al. 2004, 2009; Li et al. 2007; Van Dyk et al. 2012, 2017; Smartt 2015; Beasor & Davies 2017; Davies & Beasor 2020); a comprehensive summary of can be found in Smartt (2015) and Van Dyk (2017). The connection between RSGs and core-collapse supernovae (CCSNe) links two stellar phases between a hugely disruptive explosion, which enables studies of stellar evolution as well as the mechanisms that cause CCSN. Furthermore, as progenitors of SNe, RSG properties impact the formation of stellar mass black holes and neutron stars, themselves sources of gravitational waves through possible eventual mergers.

The next Galactic CCSN will represent a once-in-a-generation opportunity to study important progenitor-SN connections in unprecedented detail. Such CCSNe are rare, but they allow us to study neutrinos (e.g. Scholberg 2012), gravitational waves (GW; e.g. Ott 2009; Kotake 2013), and nuclear gamma rays (e.g. Gehrels, Leventhal & MacCallum 1987; Horiuchi & Beacom 2010). These observables allow us to probe far more completely inside the stellar photosphere. The neutrinos are key since they are emitted from the proto-neutron star deep within the progenitor. They are also emitted before the SN starts and the neutrinos can be used to point to the location in the sky with an error circle of a few to ten degrees (Beacom & Vogel 1999; Bueno, Gil-Botella & Rubbia 2003; Tomàs et al. 2003; Mukhopadhyay et al. 2020). These make neutrinos ideal as an early warning trigger for the SN and is the backbone of multimessenger observation strategies for CCSNe. In addition, the final stage of Si burning in massive stars emits neutrinos with $\sim 5 \times 10^{50}$ erg (Arnett et al. 1989), which can be detected for progenitors within a few kpcs (Odrzywolek, Misiaszek & Kutschera 2004; Asakura et al. 2016; Kharusi et al. 2021), acting as another layer of early trigger. Various aspects, including predictions, implementations, and detectability of the multimessenger signals of Galactic and nearby CCSNe have been explored over the years (Adams et al. 2013; Nakamura et al. 2016; Kharusi et al. 2021).

To most effectively capture this opportunity, awareness of the properties and spatial distributions of RSGs is crucial. With such knowledge, the rapid identification of the SN progenitor would

★ E-mail: healys@vt.edu

become more realistic, e.g. mirroring the strategies in the gravitational wave community with lists of galaxies for follow-up searches (White, Daw & Dhillon 2011; and more recently Dálya et al. 2018). The effective use of a pre-compiled target list would allow, among others, monitoring of the earliest light curves of the progenitor/SN, which are crucial for accurate reconstruction of the CCSN evolution and determining progenitor properties (e.g. Tominaga et al. 2011).

However, our knowledge of RSGs remains incomplete. In particular, the spatial and luminosity distributions are not well known. Spectra from massive stars are limited, and even more so are those with assigned spectral types. While the temperature scale of Galactic RSGs has been a topic of study for decades (Johnson 1964, 1966; Lee 1970; Flower 1975, 1977), and has been updated in a series of recent papers – Levesque et al. (2005, 2006) compared the strength of the TiO bands in the optical to that of MARCS's model atmospheres – the debate about the precise temperatures of Galactic RSGs is still ongoing (Taniguchi & Winered Team 2021; Taniguchi et al. 2021). It is also known that the most evolved RSGs have substantially higher levels of circumstellar extinction, but the dust sizes and distributions are not well modelled. Since dust estimations directly affect luminosity calculations, this can lead to errors in a star's bolometric luminosity, mass, and stellar radius (Beasor & Davies 2016).

While the extensive information that can be obtained from Galactic CCSNe cannot be matched by extragalactic ones, it is worth noting that RSG samples in the Magellanic clouds, M31, and M33 are estimated to be near-complete. The number of known RSGs in the LMC and SMC was initially a few tens (Feast et al. 1980; Catchpole & Feast 1981; Wood, Bessell & Fox 1983; Pierce, Jurcevic & Crabtree 2000) and increased to a couple hundred (Massey 2002; Massey & Olsen 2003; Yang & Jiang 2011; Neugent et al. 2012; Yang & Jiang 2012; González-Fernández et al. 2015) but the more recent work of Yang et al. (2019, 2021) identified an approximately 90 per cent complete sample with 1405 (SMC) and 2974 (LMC). Similarly, work done in M31 and M33 initially selected 437 (M31) and 776 (M33) candidates (Massey et al. 2006, 2007, 2009; Drout, Massey & Meynet 2012) with 255 of those confirmed to be RSGs by Massey & Evans (2016). However, Ren et al. (2019) found a lack of known faint stars motivating the identification of a near-complete sample containing 5498 (M31) and 3055 (M33) RSGs (Ren et al. 2021).

Mapping the Milky Way's RSGs has been attempted in the past. For example, those compiled with a greater focus on pre-explosion studies, including Messineo & Brown (2019) with 889 late-type bright stars of which ∼382 are RSG candidates, and Messineo (2023) with 203 bright late-type stars of which 20 are candidate RSGs. Also, lists exist that are focused more on post-explosion studies, including Nakamura et al. (2016)'s 212 stars and Mukhopadhyay et al. (2020)'s 31 stars. We build on the methods of Messineo & Brown (2019) but design our methodology to minimize losing a true RSG even at the expense of keeping more non-RSG contaminates. To further augment our list, we include a second method for search. We also compile or estimate additional stellar characteristics, e.g. variability, radius, multistar system, cluster membership, runaway status, presence of a significant magnetic field, mass-loss rate, and classification as a runaway star. We present a systematic list of Galactic binaries. Finally, we look into our final samples' angular separation compared to the angular resolution anticipated from future CCSN neutrino detections in preparation for use in multimessenger astronomy. Further discussion of Galactic RSG surveys in the literature and comparisons to our work is in Section 5.

A comprehensive list of evolved massive stars in the Milky Way galaxy will have numerous broader benefits beyond multimessenger astronomy. For example, it can be used to study the effects of massive star evolution, binary influence, as well as metallicity. RSGs trace stars with masses from about 9 to 40 $M_\odot$, i.e. ages of 4 to 30 Myr (Ekström et al. 2012; Chieffi & Limongi 2013). The binary frequency of RSGs can be used to test interaction rates when compared to unevolved massive stars. At the point of writing this paper, approximately a dozen Galactic RSG binaries are confirmed (Neugent et al. 2019). The main factor in making these improvements is having a relatively complete Galactic RSGs population that also spans various metallicities.

This paper is organized as follows. In Section 2, we compile our list of bright and cool stars and measurements of their distance, photometry, and dust extinction. We determine our most confident sample using luminosity, stellar evolution tracks, and note stars with typical RSG characteristics in Section 3. In Section 4, we discuss specific objects of interest, the sample's spatial distribution, the range of estimated radii, and mass-loss. The implications for the list and coordinated use with multimessenger astronomy (MMA) for Galactic CCSNe and massive star astronomy are discussed in Sections 5 and 6. We conclude in Section 7.

Table 1. Progression of sample size moving through steps building up to calculations of bolometric luminosity.

Cuts	Compilation based	*Gaia* based[1]
Bright late-type stars	2051	$\sim 2.2 \times 10^7$
K or M spectral type[2]	2051	3499
Matches in *Gaia*	2046	3499
Distance cut	1480	3425
Cross matches in 2MASS	1421	3410
Final RSGs[3]	555	38

Notes. [1] Includes contributions from DR2 and DR3
[2] This step only applies to the *Gaia* based method
[3] Includes 15 duplicates between the two methods

2 METHODS

We aim to determine whether a star is an RSG by using its effective temperature and bolometric luminosity. We first collect a sample of luminous late-type stars, which we define by spectral type K or M and luminosity class I. Based on spectral types, $T_{\rm eff}$ is estimated with the temperature scale for RSGs determined in Levesque et al. (2005). From there, we collect photometry measurements, model dust extinction, and estimate the intrinsic bolometric magnitude and $T_{\rm eff}$, which are crucial to determining whether the star is more likely an RSG or contamination from a non-RSG.

2.1 Data selection

We consider two data selection methods, each designed to create a starting list of stars with RSG-like properties. The first 'compilation-base' method focuses on selecting stars with predetermined spectral types matching the expectations of RSGs, i.e. a collection of K-M types stars with luminosity class I. However, spectral classifications of Galactic massive stars are relatively small in size. To remove this limitation, we use a second '*Gaia*-based' method, which focuses on obtaining stars whose position on the HR (or pseudo HR) diagram matches the expectations of RSGs. To this end, we utilize *Gaia* photometry and colour to place a cut on *Gaia* DR3 stars to obtain stars that compare to K-M stars with luminosity class I. We describe in detail the two methods below and summarize total counts in Table 1.

Table 2. Summary of late-type bright stars compiled from both method whose distance uncertainty meet the requirements detailed in Section 2.2. For stars from the compilation-based method, we list all spectral types recorded along with the mean adopted spectral type. Spectral types from Houk (1999) for stars in the *Gaia*-based sample are included with the adopted spectral type set equal to the spectral type. Alias, *Gaia* DR3 IDs, RA, Dec, parallax, and distance are included along with the $T_{\rm eff}$ determined using the adopted spectral type. The full table is publicly available at https://github.com/SNEWS2/candidate_list.

Alias	*Gaia* DR3 ID	RA	Dec	Parallax	SpType[1]	SpType_a[2]	Source[3]	r_med_geo[4]	$T_{\rm eff}$
IRAS 20315+4026	2 064 747 910 568 516 608	308.35	40.61	0.18	M0:	M0	0	3809.8	3790.0
∗ psi01 Aur	970 675 154 497 903 616	96.22	49.29	0.44	M0, K4, K5,...	M0	0, 36, 38,...	2021.5	3790.0
∗ 6 Gem	3 425 055 656 275 589 632	93.08	22.91	0.56	M2, M1, M2+,...	M0	0, 36, 38,...	1757.05	3790.0
DO 42 870	2 010 457 973 461 961 344	349.63	58.55	0.26	M1, M1	M1	0, 5	3393.6182	3745.0
'[NBM54]' 44	4 097 664 886 515 067 392	273.65	− 16.36	0.13	M1	M1	0	5085.879	3745.0
V∗ NR Vul	2 020 687 421 645 374 720	297.55	24.92	0.32	M2, M1, M1,...	K3	0, 36, 38,...	2774.4	3985.83
DO 42 870	2 010 457 973 461 961 344	349.63	58.55	0.26	M1, M1	M1	0, 5	3393.62	3745.0
CD-30 5114	5 598 579 347 402 547 072	117.05	− 30.83	0.28	K2.5	K2.5	0	3267.55	4015.0
HD 87 438	5 255 870 712 734 219 648	150.71	− 62.16	0.85	K3	K3	0	1175.17	3985.83
HD 119 796	5 865 517 646 532 509 568	206.8	− 62.59	0.25	K0, K0, K0	K0	0, 26	3600.67	4185.0

Notes. [1] List of all spectral types matched to an object and the corresponding sources are in the same order under the Source column
[2] Adopted spectral type based on the mean of SpType
[3]1 Blum et al. (2003), 2 Clark et al. (2005), 3 Clark et al. (2009), 4 Dorda et al. (2016b), 5 Dorda et al. (2018), 6 Liermann et al. (2009), 7 Negueruela et al. (2010), 8 Negueruela et al. (2011), 9 Negueruela et al. (2012), 10 Rayner et al. (2009), 11 Kleinmann & Hall (1986),12 Jura & Kleinmann (1990), 13 Humphreys (1978), 14 Elias et al. (1985), 15 Levesque et al. (2005), 16 Verhoelst et al. (2009), 17 Massey et al. (2001), 18 Messineo et al. (2014), 19 Messineo et al. (2008), 20 Mengel & Tacconi-Garman (2007), 21 de Burgos et al. (2020), 22 Beauchamp, Moffat & Drissen (1994), 23 Alonso-Santiago et al. (2017), 24 Davies et al. (2007), 25 Davies et al. (2008), 26 Keenan & McNeil (1989), 27 Alexander et al. (2009), 28 Bidelman (1957b), 29 Bidelman (1957a), 30 Halliday (1955), 31 Medhi et al. (2007), 32 Ginestet, Carquillat & Jaschek (1999), 33 Ginestet et al. (1997), 34 Fawley & Cohen (1974), 35 Garmany & Stencel (1992), 36 Humphreys (1970a), 37 Humphreys, Strecker & Ney (1972), 38 White & Wing (1978), 39 Marco & Negueruela (2013), 40 Boulon (1963), 41 Westerlund (1987), 42 Marco et al. (2014), 43 Currie et al. (2010), 44 González-Fernández & Negueruela (2012), 45 Humphreys (1970b), 46 Figer et al. (2006)
[4] r_med_geo: geometric and photometric distance estimate from Gaia DR3's parallaxes (Bailer-Jones et al. 2021)

2.1.1 *Method 1: compilation-based sample*

We begin by collecting Galactic spectral catalogues that use the Morgan–Keenan (MK) classification system (Morgan, Keenan & Kellman 1943). This includes those who took spectra in the near-infrared (Figer et al. 2006; Messineo et al. 2014), infrared (Blum et al. 2003; Verhoelst et al. 2009), *K*-band specific (Liermann, Hamann & Oskinova 2009; Negueruela et al. 2010), and optical (Levesque et al. 2005) and with low (Clark et al. 2005; Messineo et al. 2008) to high (Negueruela et al. 2011; Alonso-Santiago et al. 2017; de Burgos et al. 2020) resolution. Some look specifically at Galactic clusters including Westerlund I (Westerlund 1987; Clark et al. 2005; Mengel & Tacconi-Garman 2007), scutum-Cruz arm (Clark et al. 2009), RSGC1-3 (Davies et al. 2008; Negueruela et al. 2010), while others focused generally on stars in OB associations (Garmany & Stencel 1992; Massey, DeGioia-Eastwood & Waterhouse 2001). We set no requirement of what bands were used as indicators; some use the TiO band (White & Wing 1978; Elias, Frogel & Humphreys 1985), the Ca II triplet (Negueruela et al. 2012; Dorda, González-Fernández & Negueruela 2016b; Dorda, Negueruela & González-Fernández 2018), the CO band (Davies et al. 2007, 2008; Negueruela et al. 2012), or some combination of bands (Kleinmann & Hall 1986; Massey et al. 2001; Rayner, Cushing & Vacca 2009).

In an effort to be as complete as possible, we also included catalogues that were compilations of others (Humphreys 1978; Jura & Kleinmann 1990). Skiff (2014) is the largest such catalogue, containing 1058 791 entries, and not all entries can be found in Simbad.[1] Entries in the catalogue have been converted to the MK type where possible.

We restrict ourselves to K and M type stars with at least one classification of or including luminosity class I. We do not restrict the inclusion of spectra based on location in the sky. Special care was made to ensure that if there were repeats in original source classifications between these catalogues or with the earlier list, only one entry was included. A portion of the list can be found in Table 2.

Not all observations were unique and a single star could have a dozen classifications, so we implemented a method for adopting spectral types. For catalogues with well-studied objects, we adopted spectral types based on the classification assigned in those catalogues. We gave preference to Levesque et al. (2005) as they used both moderate-resolution optical spectrophotometry and the MARCS stellar atmosphere models fits to determine the spectral type. Thereafter, we prioritize the catalogues with well-studied classifications in Dorda et al. (2016a, 2018), Jura & Kleinmann (1990), Elias et al. (1985), and Humphreys (1978).

If none of the previous works provide spectral types, we adopt a mean spectral type weighted by uncertainties. This keeps in mind that classifications derived from fewer than the 8 TiO bands or from bands that have less characteristic behaviour for massive stars and those who have observational limitations, like Keenan & McNeil (1989), generally have larger uncertainties between ±1–2 subtypes (usually ± 0.5 subtypes for classification done by visual inspection of the whole 8 TiO band spectrum). We include White & Wing (1978), who, along with stating previous spectral classification, finds the mean spectral type from the 8-colour indices, which use a photoelectric system defined by eight narrow bands between 0.7 and 1.1 μm to determine 2D spectral classification. We do not adopt 2D spectral types but use them to inform mean values for entries with many classifications. This is accomplished by converting K0-M10 to a numerical scale, calculating the weighted average, and then rounding to the nearest half-integer, except for special cases with 4 or more entries where a single spectral type appears a majority of the time.

Initial celestial positions were taken directly from the source paper, but after combining all catalogues, some variance in RA and Dec was observed, partially due to the different epochs used. In order to improve the positions, we matched the stars listed in Table 2 to

[1]These stars are still retained in our analysis.

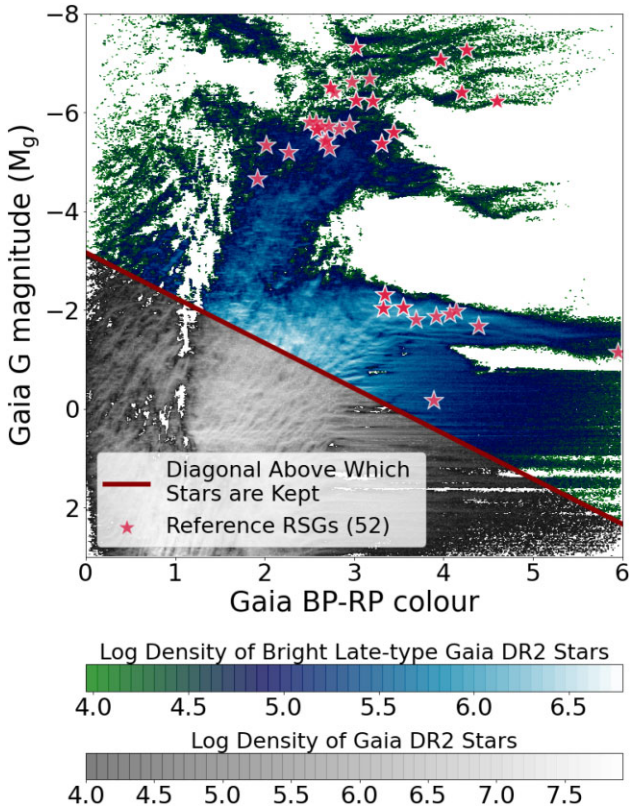

Figure 1. Log of the density distribution of *Gaia* DR2 stars in the colour–magnitude diagram of absolute *Gaia G* passband magnitudes (near-ultraviolet to near-infrared) and BP-RP colour. Overlaid are 52 stars in our reference RSG sample (see selection criteria in Section 2.1.2), plotted as red stars. Our selection cut is indicated by the solid thick dark red diagonal line (see equation 1). Stars above the cut in the green-blue shade are retained as they have temperatures and luminosity similar to those in our reference RSG sample.

Simbad based on the alias of the star and took the corresponding position with epoch J2000.0, also shown in Table 2.

In summary, our compilation-based method provided 2051 stars with either K or M spectral type and at least one classification of luminosity class I.

2.1.2 *Method 2: Gaia-based sample*

In an effort to expand our list further, we utilized the vast stellar data base of *Gaia* (DR2/DR3) and a subset of our compilation-based sample to select RSG candidates. We use *Gaia*'s *G* passband (roughly 330–1050 nm) magnitude and BP-RP (330–680 nm; 630–1050 nm) colour band for rough estimates of luminosity and effective temperature, respectively. While the absolute G magnitude does not provide total bolometric luminosity, we use it to indicate where a star would be if we had included all magnitudes from other bands; the *Gaia G* band works well for this purpose as it spans near-ultraviolet to near-infrared. Larger differences between passbands correlate with cooler stellar temperatures. The star's temperature can be inferred as the larger the difference between passbands, the cooler the star. These are shown in Fig. 1. Here, the colour indicates the log of stellar density.

We used a subset from our compilation-based sample to identify the region in the colour–magnitude diagram (CMD) corresponding to late-type bright stars. For this purpose, we used stars whose RSG status is more confident, either low uncertainty or how well-analysed it is. This includes four Galactic clusters: RSGC1, RSGC2 (Stephenson 2), RSGC3, and NGC 7419, which cover the range of expected luminosity as well as include masses $\simeq 9\,M_\odot$ to $\lesssim 25\,M_\odot$. These clusters are some of the most well-studied in terms of RSG population; most stars included in these regions have follow-up spectra, allowing us to restrict our set further to those that are or have a follow-up observation. Ultimately we use 156 stars compiled from Levesque et al. (2005), Humphreys (1978), Figer et al. (2006) (RSGC1), Negueruela et al. (2012) (RSGC2), Clark et al. (2009) (RSGC3), and Marco & Negueruela (2013) (NGC 7419). We call this our reference RSG sample.

The reference RSGs were matched to *Gaia* DR3 (DR2) objects with both *G* magnitude and estimated extinctions, which reduced the size to 30 (52) stars. The DR2 matches are shown by red stars in Fig. 1 and reveal the region where RSGs populate. The strong bimodality of the RSGs on the CMD presented in Fig. 1 likely results from the nature of stellar metallicity distribution and its effects on stellar evolution. Studies of the metallicity of the horizontal branches of globular clusters (using *Gaia* DR2 data; Gaia Collaboration 2018b and Zinn 1985) and halo stars (using *Gaia* DR2 data; Gaia Collaboration 2018b and TGAS data with RAVE and APOGEE; Bonaca et al. 2017) show the distribution is double-peaked. It is also known that the evolutionary tracks of stars are highly dependent on metallicity (El Eid; The & Meyer 2009; Maeder 2009; Langer 2012). The double-peaked metallicity distribution of stars before the RSG phase and the impact metallicity has on stellar evolution suggests the distribution of stars in the CMD is similarly bimodal as seen in Fig. 1.

Including both regions, we derive a cut to select *Gaia* stars in the CMD that are likely to be RSGs. While different cuts can be found for different samples, we choose to use the cut derived from DR2 for both *Gaia* data sets as few of our reference RSGs have estimated extinction in DR3. This limitation is primarily driven by the nature of bright stars and the high uncertainties they would likely have when methods for determining extinction values are based on training sets that exclude massive stars, as is the case for *Gaia* DR2 and DR3 (Bailer-Jones et al. 2013; Andrae et al. 2022; Delchambre et al. 2022). As our cut determined from *Gaia* DR2 is derived from absolute G mag and BP-RP colours, it is applicable to any data set containing those measurements. It includes all in the DR3-matched reference set. Our data cut is:

$$M_G \leq 0.916(BP - RP) + (-3.165) \quad (1)$$

and shown by a thick solid line in Fig. 1. Stars above the cut are bright and cool enough to be candidates RSGs. Fig. 1 shows how all our reference RSGs are above the cut. All stars are retained regardless of uncertainty; we discuss the accuracy of distance in Section 2.2. The cut makes a homogeneous sample in terms of extinction and magnitude. Still, those values are not used for later analysis, as our goal is to determine bright late-type stars homogeneously. The data sets were merged, preserving only unique values.

Our cut in the CMD gives a degree of confidence in the luminosities of selected stars. Thus, we only need to take stars with appropriate spectral types. However, our CMD provides only rough estimates for spectral types. Thus, we obtained spectral types from the Henry Draper (HD) catalogues. Over multiple publications, the HD catalogues (1918–1924), Henry Draper Extension (HDE; 1925–1936), and Henry Draper Extension Charts (HDEC; 1934) determined spectral classification and rough positions for 272 150 stars. These spectral classifications are based on the Harvard system,

which has slightly different notations for spectral types than the MK system. For consistency, we use the Michigan Catalogue of HD (MCHD) (1975–1999), which contains ∼161 000 HD stars that were reclassified to the MK system using the spectra from HD, HDE, and HDEC (Houk 1999).

Matching was done for all stars to available M and K spectral type objects from MCHD providing an additional, though not entirely unique from the compilation-based method, set of 3499 candidates. The overlap with the compilation-based method is <100 stars, reinforcing that our *Gaia*-based method provides us with valuable new candidate RSGs.

2.2 Distance related cuts with *Gaia*

We utilized the *Gaia* DR3 catalogue, which contains over 1.8 billion sources (Gaia Collaboration 2016, 2023a) to provide reliable parallaxes for both the compilation-based and *Gaia*-based samples, including uncertainties for each star. After converting coordinates from J2000 to J2016, *Gaia* matches were found within a 2 arcmin radius of each late-type star, producing objects for ∼ 96 per cent of the compilation-based method and, by design, 100 per cent of the *Gaia*-based method.

The Renormalized Unit Weight Error (RUWE), described in the technical note (Lindegren et al. 2018), is recommended by the *Gaia* team as a proxy for a good astrometric solution to a star. The unit weight error (UWE) dependence on the magnitude and colour of the source means that for consistent estimation, it needs to be re-normalized depending on colour and magnitude. RUWE is less certain for objects without colour information. Lindegren et al. (2018) recommends using RUWE ≤1.4 as a 'good' solution. However, since our list is entirely made of bright objects, they will inherently have more noise, so we choose a cut of RUWE ≤2.7 (see also Messineo & Brown 2019).

The Bayesian distance estimator `R_med_geo` is the recommended package for *Gaia* stellar distances (Luri et al. 2018; Bailer-Jones et al. 2021). Originally proposed in Bailer-Jones (2015) and further studied in Astraatmadja & Bailer-Jones (2016), estimating distances with *Gaia* becomes an inference problem that is best solved using a simple exponential decreasing space prior. With this method, non-positive parallaxes can still be used, and a bias correction is not required. We use observed parallaxes when estimating the Galactocentric coordinates as other position information, such as proper motions, are considered, as suggested in Gaia Collaboration (2018a).

Furthermore, distance errors are crucial for us to separate RSGs from impostors. The Gaia collaboration defines two errors: external which includes both random and systematic errors, and internal which is the formal errors reported in *Gaia* DR3 but only quantify the consistency of measurements.[2] The former is the total error, while the latter is not. We calculated the external parallax uncertainties as recommended by applying equation (2) to the internal uncertainties found in DR3. The external error of the parallax, $\sigma_{\overline{\omega}}$, is defined as

$$\sigma_{\overline{\omega}}(\mathrm{ext}) = \sqrt{\mathrm{k}^2 \times \sigma_{\overline{\omega}}(\mathrm{int})^2 + \sigma_s^2}, \quad (2)$$

where depending on the G mag, the values of k and σ_s are either $G \lesssim 13$: $k = 1.08$, $\sigma_s = 0.021$ or $G \gtrsim 13$: $k = 1.08$, $\sigma_s = 0.043$. With these calculations, we look for relative error, $\overline{\omega}/\sigma_{\overline{\omega}}$, and RUWE such that we retain only objects whose errors will not cause significant uncertainties in later derived quantities. Previous cuts from Messineo & Brown (2019) restricted relative error >4 to keep the difference between $1/(\omega - \omega_0)$[3] and `r_med_geo` to less than 5 per cent throughout the entire sample. In an effort to maximize final numbers while balancing quality, comparisons were made between different restrictions, shown in Fig. 2. Allowing objects whose relative parallax error >2 produces a sample whose maximum difference between distances derived from parallax and `r_med_geo` is >5 per cent, but on average, the difference is still ∼ 0.7 per cent with a median value of ∼0.2 per cent, yet almost doubles our sample size in the most favourable regions while preventing the exponentially decreasing space prior to influence `r_med_geo` to the degree that it would be dependent on parallax and the Galactic model used by Bailer-Jones et al. (2018). 4863 unique values are retained after applying the distance cut.

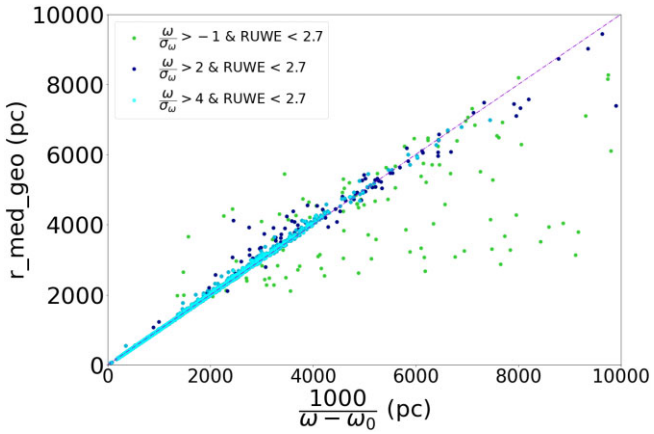

Figure 2. `r_med_geo` distance derived by Bailer-Jones et al. (2021) using Milky Way model, against parallactic distances from direct inversion of the parallaxes. As shown in the legend, those with relative error > −1 and RUWE < 2.7 are in green, and relative error > 2 and RUWE < 2.7 are in dark blue. The cyan objects have relative error > 4 and RUWE < 2.7. The pink dashed line shows the line of zero difference.

2.3 Photometry

We utilize near-infrared photometry from the Two Micron All Sky Survey (2MASS). 2MASS finished collecting 25.4 tbytes of data in 2001 February, including raw images of 99.98 per cent of our celestial sphere. The bands measured were the near-infrared (NIR) J (1.25 μm), H (1.65 μm), and K_s (2.16 μm) of which errors were calculated and produced for the data set which includes images from almost the entire sky. All images were taken through either Mount Hopkins, Arizona's and Cerro Tololo, Chile's 1.3 m diameter telescopes both with 7.8 s time accumulated for each sector (Skrutskie et al. 2006).

Using ESA pre-crossmatched best neighbour and good neighbourhood list, available 2MASS Point Source Catalogue (Skrutskie et al. 2006) matches were found for > 99 per cent of stars that had a *Gaia* DR3 ID, providing a near-complete sample of JHK_s measurements and their associated uncertainties. The K_s magnitudes range from −2 to 16.3 mag with a median value of 4.3 mag. Where available, we also include 2MASS values for the blue, visual, or red magnitude of the associated optical source.

[2] https://www.cosmos.esa.int/web/gaia/dr2-known-issues#AstrometryConsiderations

[3] Parallax zero point from Lindegren et al. (2021).

2.4 Dust

In Messineo et al. (2005), dust extinction of RSGs was calculated by using the extinction power law with an index of 1.9 and the intrinsic coloūrs expected for each spectral type. However, RSGs in general show excess circumstellar extinction to those of OB stars in the same regions (Massey et al. 2005), causing the extinction ratios to differ from those of the main sequence or other stars. This increase in extinction for brighter massive stars is also seen in Neugent et al. (2020), which takes direct measurements of A_V for a sample of RSGs in M31.

While a linear relationship between intrinsic colour, $(J-K)_0$, and effective temperature works well for RSGs, metallicity in the models causes discrepancies as well as unlikely large extinction values. We also have to take into account that a large portion of our sample's $T_{\rm eff}$ is based on a mean spectral type. Deriving dust based on $T_{\rm eff}$ and intrinsic magnitude means not only would we need to propagate the uncertainties of $T_{\rm eff}$ and observed photometry, but we would also have to deal with the dependence between the two when calculating the uncertainties of intrinsic magnitudes. This method would keep us from treating our uncertainties as uncorrelated, complicating our error propagation. For these reasons and those described in the next section, we use Galactic dust maps to estimate reddening while keeping the extinction ratios from Messineo et al. (2005).

2.4.1 3D dust map

In recent years, the development of interstellar dust extinction maps has improved to three dimensions spanning many kiloparsecs. We use the combination MWDUST[4] created by Bovy et al. (2016) and later updated to replace Green et al. (2015) with Green et al. (2019). While there are others based on modelling stellar photometry (e.g. Marshall et al. 2006; Sale et al. 2014; Green et al. 2019), which would be ideal for our use with 2MASS photometry, none provide results for the entire sky that we need.

The combination of Bovy et al. (2016) starts with Marshall et al. (2006) based on 2MASS passbands and augments with Drimmel, Cabrera-Lavers & López-Corredoira (2003) based on dust distribution fit to COBE DIRBE data. Bovy et al. (2016) unified the projection of Marshall et al. (2006), Green et al. (2015), and Drimmel et al. (2003) to HEALPIX; note however the resolutions are variable. Collectively, Bovy et al. (2016) provides full sky coverage and preserves small-scale structures in the dust extinction.

As our sample focuses on RSGs, we modified some constants used to transform between bands which are used in the maps so that they fit the extinction transformation equation found in Messineo et al. (2005), specifically

$$\frac{A_{K_s}}{A_V} = 0.092, \quad \frac{A_H}{A_V} = 0.153, \quad \frac{A_J}{A_V} = 0.263 \tag{3}$$

$$R_V = \frac{A_V}{E(B-V)}, \tag{4}$$

where $R_{\rm V} = 3.1$. Massive stars, however, can have additional attenuation due to local extinction. For example, studies have found values of 3.6 (Lee 1970; McCall 2004) or 4.2 (Massey et al. 2005), and Massey et al. (2005). Additional dust is a major source of systematic uncertainty, but we can obtain some estimates of their impacts. In the sample of Galactic RSGs from Levesque et al. (2005), approximately 15 per cent of those with estimations for V band extinction from spectrophotometry differ significantly – here quantified as impacting our classification of a star as an RSG or not (see Section 3.3) – from estimations based on $R_{\rm V} = 3.1$. While their use of moderate-resolution SEDs significantly reduces the chance of discounting high-extinction RSGs, dust attenuation in the NIR is less than that of the optical or lower wavelengths, minimizing our sensitivity to extinction estimations and improving our ability to retain RSG with excess reddening. For these reasons, we conservatively use $R_{\rm V} = 3.1$, giving us a final sample of stars with either approximately correct or underestimated luminosity. While this makes our sample biased against RSGs with extra extinction, any higher value of $R_{\rm V}$ would only increase the luminosity of stars and hence increase our sample size.

As Marshall et al. (2006) uses $A_{K_s} = 0.089 A_V$, we make the appropriate correction to match the above. The Green et al. (2019) map is intended to provide reddening in a similar unit as $E(B-V)_{\rm SFD}$ (Schlegel, Finkbeiner & Davis 1998) which can be covered to $E(B-V)$ by multiplying 0.884, the constant found in Schlegel et al. (1998) and then moving through the equations above to get A_{Ks}. While Drimmel et al. (2003) is normalized to $E(B-V)_{\rm SFD}$, MWDUST appropriately converts to A_V.

Since MWDUST does not provide uncertainties, we estimate them by comparing different maps. We used DUSTMAPS, a python package that can be used to query several commonly used maps of interstellar dust, including 2D maps such as Schlegel et al. (1998), Planck Collaboration XVI (2014), Lenz, Hensley & Doré (2017), and 3D maps such as Marshall et al. (2006) and Green et al. (2015). If Marshall et al. (2006) was the map with the largest impact on final MWDUST extinction value, we pulled the uncertainties from DUSTMAPS as they were included in the DUSTMAPS module. For Green et al. (2019), values were not directly provided by DUSTMAPS , so we followed the method in Green et al. (2015) and took the uncertainty to be half the difference between the 84th and 16th percentiles. While Drimmel et al. (2003) does not provide uncertainties, they point to López-Corredoira et al. (2002) who estimates the uncertainties in the K_s band extinction to be less than 0.015, so all objects where Drimmel et al. (2003) largely determines extinction value have the error set to 0.015 for simplicity. Even though this reduces the confidence of calculated uncertainty for relevant objects, it is < 25 per cent of the final sample. These uncertainties also required the matching conversion applied to the extinction above.

The values derived from 3D Galactic dust extinction maps are noticeably different from those calculated using intrinsic colours from $T_{\rm eff}$. We summarize the details in Section 4.7.

3 RESULTS

We determine our most probable RSGs by using the parameter space of $\log(L/L_\odot)$ versus $T_{\rm eff}$. To this end, we first determine the luminosity and $T_{\rm eff}$, then compare them to simulated evolutionary tracks for massive stars, and finally determine the most likely regions by considering the contamination from AGB stars.

3.1 Luminosity

Using the extinction method described in Section 2.4, we estimate the absolute magnitude in the $K_{\rm s}$ band based on the de-reddened 2MASS $K_{\rm s}$ magnitude and the distance moduli derived from the Bailer-Jones et al. (2018) geometric distance estimates. Bolometric corrections determined by Levesque et al. (2005) were matched to stars based on their spectral type and then applied to the absolute $K_{\rm s}$ magnitude, yielding the bolometric magnitude. From the bolometric

[4] http://github.com/jobovy/mwdust

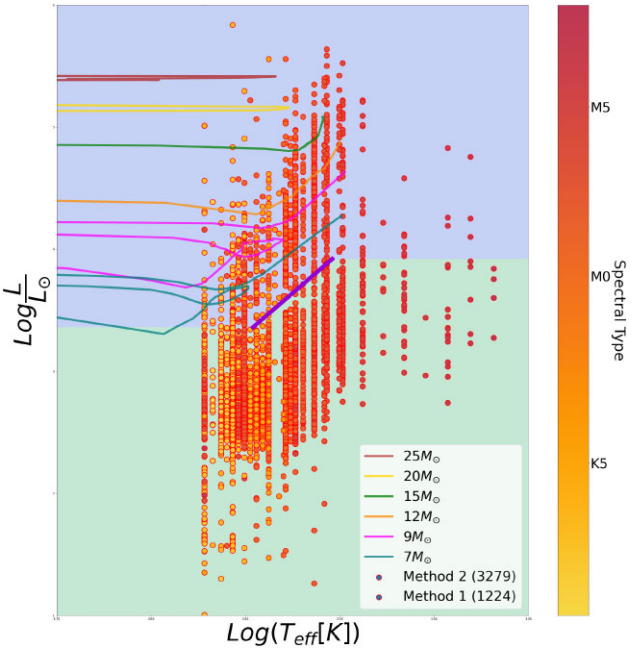

Figure 3. Luminosity versus $T_{\rm eff}$ of stars in both methods, coloured by their intrinsic $K_{\rm s}$ magnitude. Stellar tracks from models at solar metallicity and including rotation from Ekström et al. (2012) are shown for different ZAMS masses, as labelled. The thick purple diagonal line recreates the ascending track from the 7 $M_\odot$ progenitor, shifted to account for uncertainties in $\lesssim 7-9\,M_\odot$ mass stellar tracks.

magnitude, we determined bolometric luminosities relative to the sun, $\log(L/L_\odot)$. By design, all uncertainties can be treated as independent, so we propagate errors of bolometric luminosities using those of $T_{\rm eff}$, 2MASS photometry, dust extinction, and geometric distance estimates.

3.2 Comparison to evolutionary tracks

With $T_{\rm eff}$ and luminosity, we can compare the distribution of stars in the H-R diagram against evolutionary tracks predicted for massive stars. In Fig. 3, we show our sample against tracks of Ekström et al. (2012) for rotating stars computed at solar metallicity (z = 0.014) over the mass range 7–25 $M_\odot$. For solar metallicity, anything above 25 $M_\odot$ is not cool enough to truly be called RSGs, and anything below 7 $M_\odot$ would be too small. While these evolutionary tracks do not account for binary evolution, the tracks are still appropriate as binary evolution does not greatly affect the location of RSG on the HR diagram; Levesque (2017) succinctly showed this in their fig. 8.3 which shows a comparison between the single-star Geneva and BPASS binary evolutionary tracks (Eldridge & Stanway 2016; Eldridge et al. 2017) [fig. 7 of Levesque (2018) also supports this].

The tracks for stars of 7 and 9 $M_\odot$ are particularly uncertain as their evolutions are not well understood, and this can be seen as these lines cover wider ranges in luminosity and are different shapes from those of higher mass. If these lines are used as cuts, it is possible that we would exclude true RSGs from our list. To take this uncertainty into account, we follow Messineo & Brown (2019) and use a diagonal cut base on the 7 $M_\odot$ track but shifted down and right to the ascending track. This line, plotted in thick purple in Fig. 3, gives us a limit for how faint or red a star could be and still be a candidate RSG:

$$\log(L/L_\odot) = 51.3 - 13.33 \times \log(T_{\rm eff}), \quad (5)$$

where $\log(T_{\rm eff})$ varies from 3.54 to 3.6 (or M4 to K1, based on Levesque et al. 2005). As RSGs candidates should be on or between the stellar tracks, with uncertainties taken into account, we can define approximate regions for RSGs. In the following, we determine this in more detail by also considering contamination.

3.3 Identifying regions

The main contamination for RSGs is AGB stars. AGBs have lower initial masses and spend more time on the main sequence; however, in their extreme cases, those that are oxygen-rich or carbon-rich increase in luminosity at a warmer temperature than the average AGB and will cross into the areas that we deem regions for RSG. To quantify this, we compare the distribution of Galactic AGBs and RSGs in the HR diagram. We sourced from the literature Galactic AGBs surveys that include values for both $T_{\rm eff}$ and Luminosity (or $M_{\rm bol}$) (Blum et al. 2003; Milam et al. 2009; McDonald et al. 2011; Groenewegen 2022) to quantify how much each region is contaminated. We include a list of extreme AGBs (Groenewegen 2022), including both C-rich and O-rich, as these would most likely be incorrectly selected as RSGs. The extreme AGBs list includes a small fraction of AGBs supplemented from the Magellanic Cloud. Altogether, we compile 377 AGBs to compare to the reference RSG sample compiled in Section 2.1.2.

The results are shown in Fig. 4. Based on these, we define five regions. The percentages of AGBs and RSGs in these regions are given in Table 3. The five regions are:

(i) **Region A (Blue)**: defined by $\log(\frac{L}{L_\odot}) \geq 4.76$. It has little contamination: only 1.7 per cent of the reference AGBs are in region A, while 55.4 per cent of the reference RSG population is here. Compared to stellar tracks, region A contains high mass RSGs with $\geq 15\,M_\odot$.

(ii) **Region B (Purple)**: defined by $\log(\frac{L}{L_\odot})$ between 3.92 and 4.76 and whose spectral type is earlier than M4, $T_{\rm eff} \geq 3535$ K. It is still RSG-rich (39.2 per cent of the reference RSGs) but has more contamination than region A (13.9 per cent of reference AGBs). Region B contains intermediate mass RSGs with masses between 15 and 9 $M_\odot$, which fall along well-defined stellar tracks.

(iii) **Region C (Red)**: defined by $\log(\frac{L}{L_\odot})$ between 3.36 and 3.92 and is bluer than equation (5). It contains intermediate-mass AGBs (4.9 per cent of AGBs), and as discussed below, lower mass 9$M_\odot$ RSGs should be in this region but biased against observation (0 per cent of RSGs).

(iv) **Region D (Orange)**: defined by $\log(\frac{L}{L_\odot})$ between 3.92 and 4.76 and anything $T_{\rm eff} \leq 3535$ K. Compared to region B it contains a larger fraction of AGB contamination (34.7 per cent of reference AGBs) and a smaller fraction of RSGs (5.4 per cent of reference RSGs).

(v) **Region E (Green)**: defined by $\log(\frac{L}{L_\odot})$ between 3.36 and 3.92 and redder than equation (5) or anything with $\log(\frac{L}{L_\odot}) < 3.36$. It contains a large fraction of the reference AGBs (44.8 per cent) and none of the reference RSGs. Region E stars are either too red or too dim to be RSGs of any mass.

The reference RSGs along with our reference AGBs illustrate an issue in massive star studies, which is that we lack stellar tracks certain enough and photometric characteristics that could distinguish between 7 and 9 $M_\odot$ RSGs and contamination from lower mass stars and extreme AGBs (Siess 2006; Poelarends et al. 2008). The best options beyond modelling and photometry also fail in certain cases; observation of spectral lines sensitive to surface gravity fail for cool emission spectra, high-resolution follow-up is not realistic

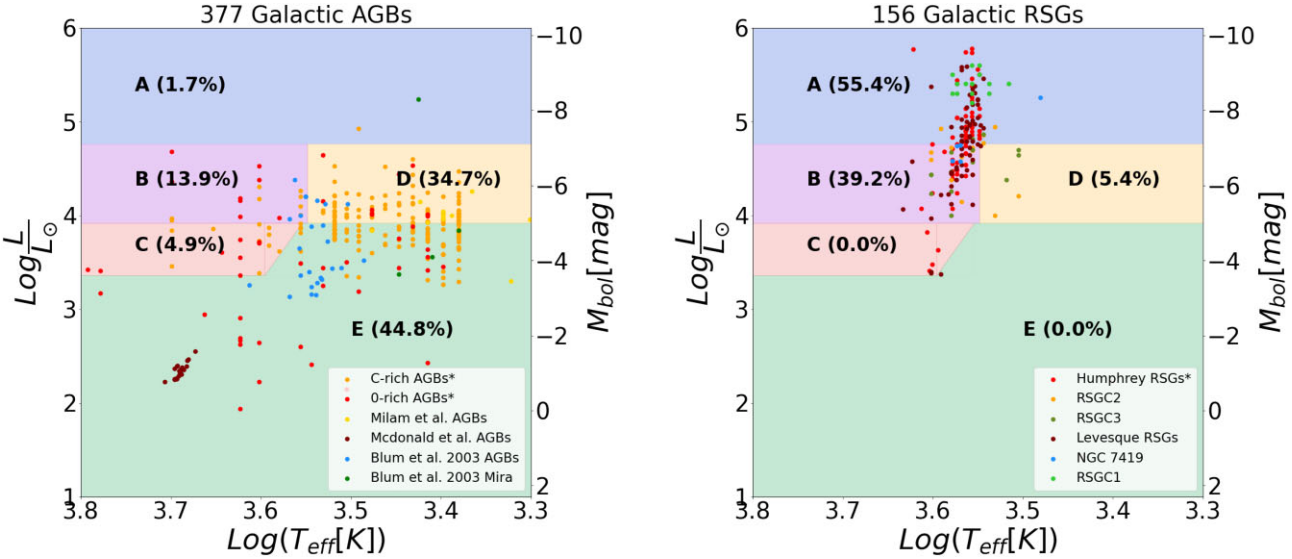

Figure 4. Left: 377 Galactic AGB, including a set of extreme AGBs from the literature (Blum et al. 2003; Milam, Woolf & Ziurys 2009; McDonald, Johnson & Zijlstra 2011; Groenewegen 2022); see Section 3.3 for further details. In each of the regions A–E, we label the percentage of the AGB sample residing in that region. Right: our 156 reference RSGs (Humphreys 1978; Levesque et al. 2005; Figer et al. 2006; Clark et al. 2009; Negueruela et al. 2012; Marco & Negueruela 2013), compiled under the guidelines set in Section 2.1.2. The percentages indicate the fraction of the reference RSG residing in each of the regions A–E.

Table 3. Percentages of the reference RSGs and AGBs in the five regions labelled A∼E. For each region, the per cent of AGBs known to be extreme, either carbon or oxygen, is also stated in parentheses. Note that percentages in region C are likely severely underestimated as there is a bias against confirming RSGs or AGBs (see Section 3.3).

Region	AGBs (Known extreme AGBs)	RSGs
A (Blue)	1.7 per cent (80 per cent)	55.4 per cent
B (Purple)	13.9 per cent (87.5 per cent)	39.2 per cent
C (Red)	4.9 per cent (89.0 per cent)	∼0 per cent
D (Orange)	34.7 per cent (0.0 per cent)	5.4 per cent
E (Green)	44.8 per cent (38.8 per cent)	∼0 per cent

logistically for large data sets, and use of maser emissions requires circumstellar masers to distinguish between supergiant and giant stars (Levesque 2017). Even in this list of well-studied RSGs, almost none have masses below 9 $M_\odot$ even though these should be more common than higher mass RSGs. This results from the prevailing selection criteria, similar to that in Massey & Olsen (2003), which applies a conservative lower limit and filters out lower mass RSGs. Ultimately, we similarly remove Region C even though it should contain low-mass RSGs.

3.4 The catalogue

We show in Fig. 5 our five regions and our sample combining the compilation-based and *Gaia*-based methods. We keep stars in Regions A and B for our final RSG list. This results in 134 and 436 stars, respectively. However, we can also include stars that satisfy the region cuts after consideration of errors. We include distance, photometry, dust extinction, and effective temperature as errors. These stars are listed in their original region identifier, meaning C, D, or E (see Appendix A for a complete column listing of the catalogue). Still, they are included as 'likely' RSGs in the final catalogue due to uncertainties. This adds another 62 stars, primarily from Region C.

3.5 Characteristics flags

We add additional flags that give extra insight into how likely an object is an RSG, going beyond the required luminosity and temperature cuts. The statistics of these flags are shown in Table 4.

3.5.1 Clusters

Due to the dense molecular cloud that massive stars are born in, RSGs often form as part of a cluster or OB associations, so RSGs searches are often restricted to a specific cluster. We thus search the literature to see if each star is a member or candidate member of any Milky Way cluster. We include the cluster name, any radial velocity derived from cluster dynamics, and any cluster details, like age, approximate distance, and mass, into the catalogue if available. The main clusters found include Stephenson 2 (RSGC2), PER OB1, and CAR OB1.

3.5.2 Multistar systems

Like OB associations and clusters, the dynamics of the molecular clouds are appropriate for forming binary systems. Considering the significant binary fraction for main-sequence massive stars, once a massive star reaches mass transfer at the Hayashi limit, it is likely that this will cause an increase in the binary fractions of massive stars. To what extent it increases depends on the theoretical treatment of RSGs. It is almost certain that the limitation of observations and the rarity of RSGs are the causes of so few known binaries.

We thus include a flag for stars that have evidence of interactions with a companion. The catalogue contains a column to flag binary and multistar systems and a column detailing if the spectra show a binary (Spectral Binary), if *Gaia* DR3 has identified it as a multiple object system (`non_single_star`), or if the literature defines it as such. There is also a corresponding reference column that will give the relevant reference.

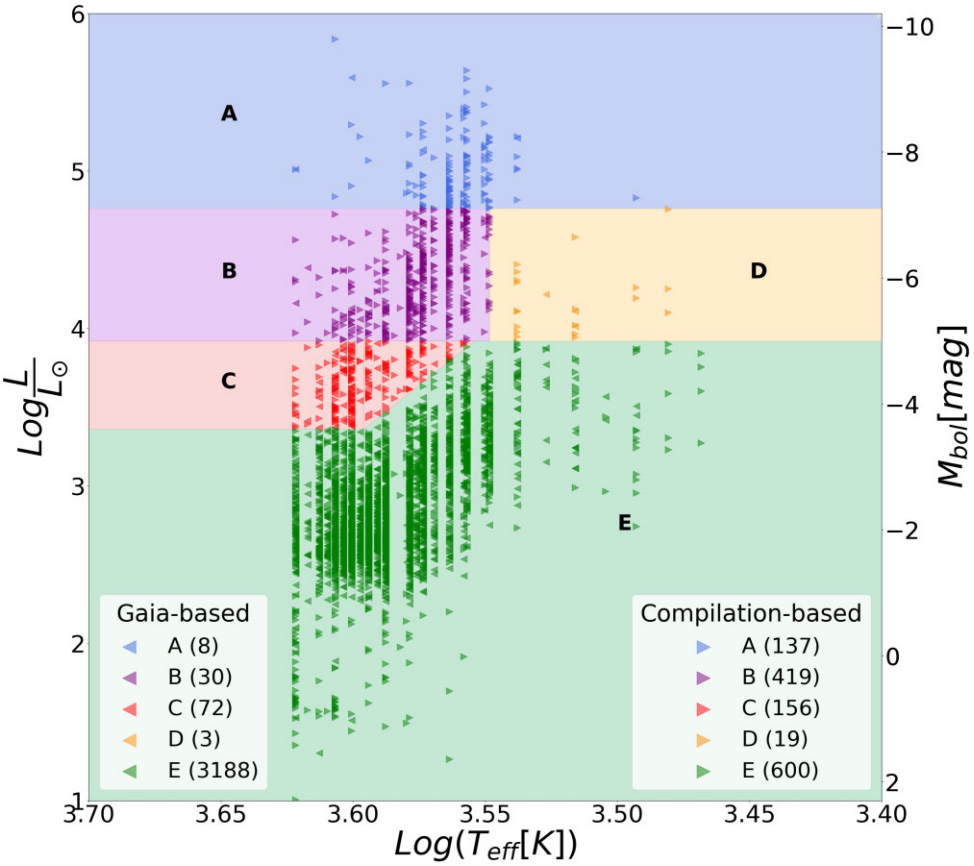

Figure 5. Luminosities versus $T_{\rm eff}$ values of the compilation-based method (arrows pointing right) and the *Gaia*-based method (arrows pointing left), for stars with relative error > 4 and RUWE < 2.7. Stars within Region A (blue) and Region B (purple) are highly probable RSGs. Region B contains some contamination from AGBs. Region C (Red) contains intermediate-mass AGBs and late M and K type stars with solar masses around 9$M_\odot$. As discussed in Section 3.3, lower mass RSGs should be in this region. Region D (Orange) and Region E (Green) stars are either too red or too dim to generally be RSGs of any mass, so they are unlikely regions to find RSGs. The number of stars for each region, not accounting for repeats between methods, is shown in the legend in parentheses.

Table 4. Breakdown of characteristics for highly probable RSGs included in the final catalogue separated into Region A (138 stars) and Region B (460 stars). Close RSGs are those whose proximity, extended radius, and/or brightness lead to poor or no measurements in *Gaia* and were manually added to our catalogue as described in Section 4.1.1.

Region	OB Association & clusters	Variability (spectra or photometry)	Binary (spectra or photometry)	Measured magnetic field	Runaway
Region A	37	137	11	1	1
Region B	62	312	60	2	0
Close RSGs	7	12	4	10	3

3.5.3 Variability

RSGs are expected to be radial pulsators with luminosity-dependent pulsational periods (Stothers 1969, 1972; Heger et al. 1997; Guo & Li 2002) leading to photometric variation. Mass-loss rates have been measured up to $10^{-5}\,M_\odot\,yr^{-1}$ (Beasor & Davies 2016) and are another driver for variability. Spectroscopic variability is affected by the dynamics of their outer layers, like extended atmosphere and optical depth effects near the Hayashi limit or convection, pulsation, and mass-loss. While the dominant driver responsible for this variation is unknown, it is an important characteristic of RSGs. We, therefore, included a flag for any object which is designated as a variable star, either in the literature, AAVSO, ASAS-SN (Shappee et al. 2014; Jayasinghe et al. 2020), or through *Gaia* DR2/DR3's photometric variability flag. The latter uses statistics, time-series, and data mining analysis on *Gaia* G, G_{BP}, G_{RP} photometry as well as parallaxes and positions (Holl et al. 2018) and using statistical and machine learning methods built from a global revision of major published variable star catalogues (Eyer et al. 2023).

4 DISCUSSION AND INTERPRETATIONS

4.1 Specific objects

4.1.1 RSGs which are not in Gaia DR3

Even though *Gaia* has a large magnitude range $G \sim 3$ to 21 mag, for any star with G mag <5, the brightness could lead to saturation and subsequent systematic errors in parallax. This happens since *Gaia* astrometric measurements use the stars' magnitudes in part to self-calibrate, so this becomes a problem as bright stars are scarce

(Lindegren et al. 2018). Also, the extreme widths of massive stars can limit the accuracy of *Gaia*'s parallax measurement. For stars with magnitudes bright and radii wide enough to have large enough errors to be removed from our pipeline but are generally accepted as RSGs in literature, we reintroduce them into our sample. There are 12 stars in this category. It includes θ Del, μ Cep, S Per, VX Sgr, and NML Cyg who are in *Gaia* DR3 but whose measurements are saturated and accuracy is reduced below our threshold, and alf Ori (aka Betelgeuse), alf Her, alf Sco, eps Peg, ζ Cep, and lam Vel who are not in *Gaia* DR3 due to some combination of their distance, brightness, and radii. We also include VY CMa, whose brightness and distance should not lead to oversaturation but is excluded as its radius, one of the widest RSGs in our galaxy, hinders accurate distance measurements.

As the above list is not measured with *Gaia* DR3, we do not use our pipeline to determine their bolometric magnitude or luminosity. Instead, we used values determined throughout the literature. These papers are denoted in the catalogue, and a full list can be found in Appendix B. While we tried to fill as many columns as possible for each non-*Gaia* object, this was not possible for some columns, especially those from *Gaia*. A list is provided in a single reference column for objects whose values come from multiple sources.

4.1.2 MY cep

The use of stellar tracks and reference RSGs/AGBs to determine our regions for possible candidates resulted in MY Cep being removed from our list, not because it does not have a high enough luminosity, but because its $T_{\rm eff}$ is too cool. However, MY Cep is generally acknowledged as an RSG (Levesque et al. 2005; Mauron & Josselin 2011; Humphreys et al. 2020) and it makes sense to keep it when considering the uncertainty in $T_{\rm eff}$.

4.2 Runaway RSGs

Blaauw (1956a, b) discovered a sample of OB stars with significantly higher space velocities than their surroundings, denoted runaway stars (RWs). RWs were first theorized to originate from binary systems whose primary undergoes SN and shoots the secondary out, creating their peculiar velocities. However, this has been disproven as a primary mechanism (Gies & Bolton 1986). Other explanations hypothesize their existence from dynamical ejection (Leonard & Duncan 1990) or interactions with massive black holes (Capuzzo-Dolcetta & Fragione 2015; Fragione & Capuzzo-Dolcetta 2016). Estimates for OB stars with peculiar radial velocities $\gtrsim 40\,{\rm kms}^{-1}$ reach as high as 50 per cent of the population (Gies & Bolton 1986). However, few RW massive stars are known. Galactic RW RSGs include those identified due to the presence of bow shocks: Betelgeuse (56 ${\rm kms}^{-1}$; Noriega-Crespo et al. 1997; Mackey et al. 2012, μCephei (22 ${\rm kms}^{-1}$; Cox et al. 2012), and IRC -10414 (70 ${\rm kms}^{-1}$, Gvaramadze et al. 2013) and by Kinematical data from the *Gaia* DR2 catalogue: HD 137 071 (54.1 ${\rm kms}^{-1}$; Tetzlaff, Neuhäuser & Hohle 2011; Comerón & Figueras 2020) which interestingly is both the only known K-type and whose proposed velocity evolution favours the non-dominant mechanism of ejection due to SN (Comerón & Figueras 2020). All of these are included in the final sample.

4.3 Presence of magnetic field

While the extent to which magnetic fields can contribute to total mass-loss in RSGs is unknown, perturbation of fields with strength greater than several Gauss could have effects through the production of Alfven waves (Hartmann & Avrett 1984; Charbonneau & MacGregor 1995; Vidotto & Jatenco-Pereira 2006). There have been several Galactic RSGs with measured magnetic fields, including $\sim$1 G in Betelgeuse (Aurière et al. 2010; Tessore et al. 2017). Observations of surrounding circular polarization from Zeeman-splitting suggest a surface magnetic field as strong as 4 G for VX Sgr (Vlemmings, van Langevelde & Diamond 2005), $\sim$1 G for 32 Cyg, and $\sim$2 G for λ Vel (Grunhut et al. 2010). Tessore et al. (2017) detected $\sim$1 G from CE Tau and μCep, and several G in α^1 Her similar to the magnetic fields of AGBs. Measurements of VY Cma show disagreement with estimations from H_2O maser observation ranging from 90 to 180 mG (Vlemmings, Diamond & van Langevelde 2002) and estimations based on linear polarization suggesting a lower limit of $\sim$10 G (Shinnaga et al. 2017). Discussion detailing possible reasons for this disagreement are presented in Shinnaga et al. (2017). Non-detections of post-RSG stars have also been made, such as yellow SG (YSG) ρ Cas (Tessore et al. 2017), which suggests either a very weak magnetic field or its dissipation, giving insight into the stellar evolution of RSGs that evolve back to warmer temperatures.

4.4 Spatial distribution

The current collection of Galactic RSGs is still highly incomplete, with little known about the total spatial distribution (see e.g. Davies et al. 2009; Messineo et al. 2016). Even with our catalogue being the largest collection, it only extends out 12.9 kpc when the radius of the Milky Way is $\sim$ 30 kpc. Fig. 6 shows the spatial distribution of our catalogue. In the right panel, we compare with the spatial distribution of other catalogues in the literature: Nakamura et al. (2016) uses less stringent luminosity cuts but still reaches approximately the same distance, and Mukhopadhyay et al. (2020) where the inner Galactic Centre's RSGs and Blue SGs are represented but only goes out to $<$ 1 kpc. Note that we see a more prominent dearth of stars around the solar system, driven by the saturation of *Gaia* photometry (see Section 4.1.1).

The driving factor for the lack of stars beyond 12.9 kpc comes down to the availability of spectra. Even in Skiff (2014), one of the largest collections of Galactic stellar spectra, only $\sim$0.3 per cent meets the most basic spectral characteristics for RSGs. As the determination of spectral type from spectra for RSGs involves either labour, limitations to sample size, or reduction of confidence, RSGs searches have been limited by pointing in the direction of OB associations or clusters, which generally have a higher population of RSGs. However, for inner Galactic supergiants, only $\approx$ 2 per cent are associated with stellar clusters (Messineo et al. 2017). The spectra of RSGs are not only observationally limited but also lack well-defined spectral standards. This is especially true of K-type stars, which are often broken into late and early K-type stars rather than subtypes.

Even after locating candidates, intrinsic characteristics that help determine whether it is an RSG (e.g. pulsation properties and chemical abundances) are not easy to obtain. As discussed in Section 3.3, reliable confirmation is also difficult because the colours of RSGs are not unique and match those of giant late-type stars, specifically from low masses to super-AGBs of 9–10 $M_\odot$.

These issues all lead to the number of Galactic late-type stars of class I being less than $\sim$1000, and, when not considering our new catalogue, $\sim$400 RSGs known throughout various surveys. Major catalogues like Humphreys (1978) lists 92, Elias et al. (1985) lists 90, Levesque et al. (2005) analysed the spectra of 62, Jura & Kleinmann (1990) lists $\sim$135, even though more than $\sim$5000 RSGs are predicted by Gehrz (1989).

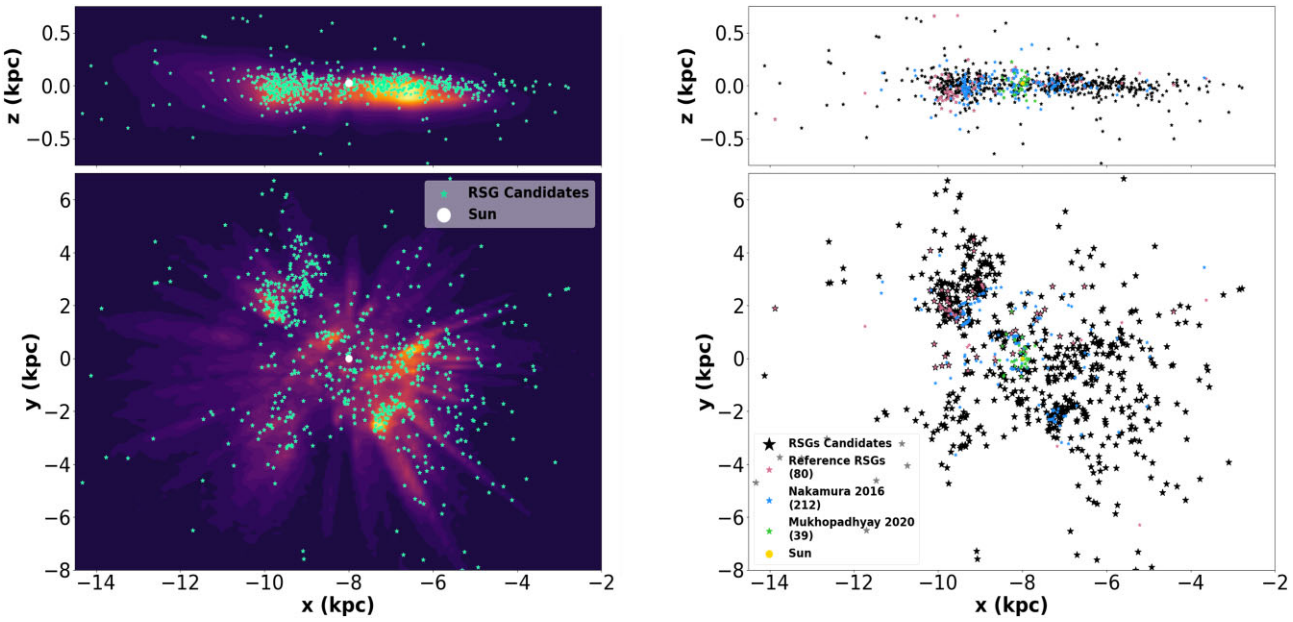

Figure 6. Left panel: Our final RSGs (teal stars) in Galactocentric coordinates compared to a population of inner Milk Way young stars (shaded based on stellar density from a 2D histogram using cells of 150x150 pc for y versus x and 150x115 pc for z versus x) on the upper main sequence selected from *Gaia* DR3 based on methods of Gaia Collaboration(2023b) whose density distribution reconstructs the spiral arms of the Milky Way, specifically, Perseus arm, Orion spur, and Sagittarius arm. The Sun's location (8, 0, 0) is marked in white. Right panel: Our RSGs catalogue (large black stars) compared to previous studies: Nakamura et al. (2016) (small light blue stars), Mukhopadhyay et al. (2020) (small green stars), and reference RSGs (small pink stars). The Sun location (8, 0, 0) is marked in yellow. The number of stars is shown in the legend in parentheses.

4.5 Radii range

The expanse of RSG radii makes measurements challenging as it limits the observational effectiveness of interferometric determinations and requires sufficiently accurate distances. For the several dozen stars with well-measured radii, comparisons to estimates from $L = 4\pi\sigma R^2 T_{\rm eff}^4$ show good agreement (Van Belle, Creech-Eakman & Hart 2009; Wittkowski et al. 2012; Arroyo-Torres et al. 2013, 2015; Wittkowski et al. 2017). Solving the equation for the radius of Betelgeuse, $\sim 855\,R_\odot$, compares well to interferometric measurements (Dolan et al. 2016) $\sim 890\,R_\odot$, especially as there is variation depending on observed wavelength, treatment of asymmetries, among other things (Townes et al. 2009). Based on this simple but effective relationship, we provide radii for all stars in our catalogue, resulting in a range of $10^{1.38}$ to $10^{3.28}\,R_\odot$.

4.6 Mass-loss rates

For massive stars, more than half of their mass-loss happens after the main sequence, with RSGs losing between 10^{-7} and $10^{-3}\,M_\odot yr^{-1}$ (van Loon et al. 2005; Mauron & Josselin 2011). Observations of CSM around type II SNe suggest that mass-loss during the final stages of the RSG phase is accelerated. Förster et al. (2018) surveyed 26 SN II within hours of their discovery and obtained optical light curves from High Cadence Transit Survey (HiTS) (Martínez-Palomera et al. 2018) that when compared to detailed models suggest density profiles consistent with $> 10^{-4}\,M_\odot yr^{-1}$. Confined dense CSM was confirmed to surround SN2013fs that was estimated to be ejected during the final $\sim$1 yr prior to explosion at a rate $\sim 10^{-3}\,M_\odot yr^{-1}$ (Yaron et al. 2017). However, with the dominant mechanism for significant mass-loss unknown and explanations incomplete, derivations of general relations are restricted to observations and limited modelling. While there are some discrepancies between different mass-loss rate relations, we estimate the mass-loss of our RSG candidates based on van Loon et al. (2005), which gives

$$\log_{10}(\dot{M}) = -5.5 + 1.05\log_{10}\left(\frac{L}{10000 L_\odot}\right) - 6.3\log_{10}\left(\frac{T_{\rm eff}}{3500{\rm K}}\right) \quad (6)$$

based on observations of a small sample of M-type stars and the assumption of a dust-driven wind model, most applicable to dust-enshrouded RSGs and oxygen-rich AGB stars. We find a range of $10^{-7.76}$ to $10^{-3.87}\,M_\odot yr^{-1}$ in our sample.

4.7 Dust extinction method comparison

In Section 2.4, we discuss our reasoning for departing from previous methods, which use observationally determined intrinsic colours for different spectral types of massive stars and working backwards to determine their dust extinction. However, when a comparison is made with the previous method, our 3D dust map, and other dust maps, we see differences significant enough for us to outline here. We compare six different methods of estimating dust: Schlegel et al. (1998), Marshall et al. (2006), Schlafly & Finkbeiner (2011), Sale et al. (2014), Planck Collaboration XVI (2014), Green et al. (2019), and Delchambre et al. (2022). We also explore how the calculations of bolometric luminosity would shift depending on the method used for extinction. Fig. 7 shows comparisons of dust corrections, spanning 3D dust maps, MWDUST, and the use of intrinsic colours of massive stars (ICMS). The close alignment to the 1-to-1 line, shown dashed in pink, for Marshall and Green results from MWDUST predominately using those two maps for their HEALPIX extinction map. We see that MWDUST produces a smaller spread across the board and generally has smaller differences from the average values as well. In Fig. 8 we show how they impact our determined stellar luminosities.

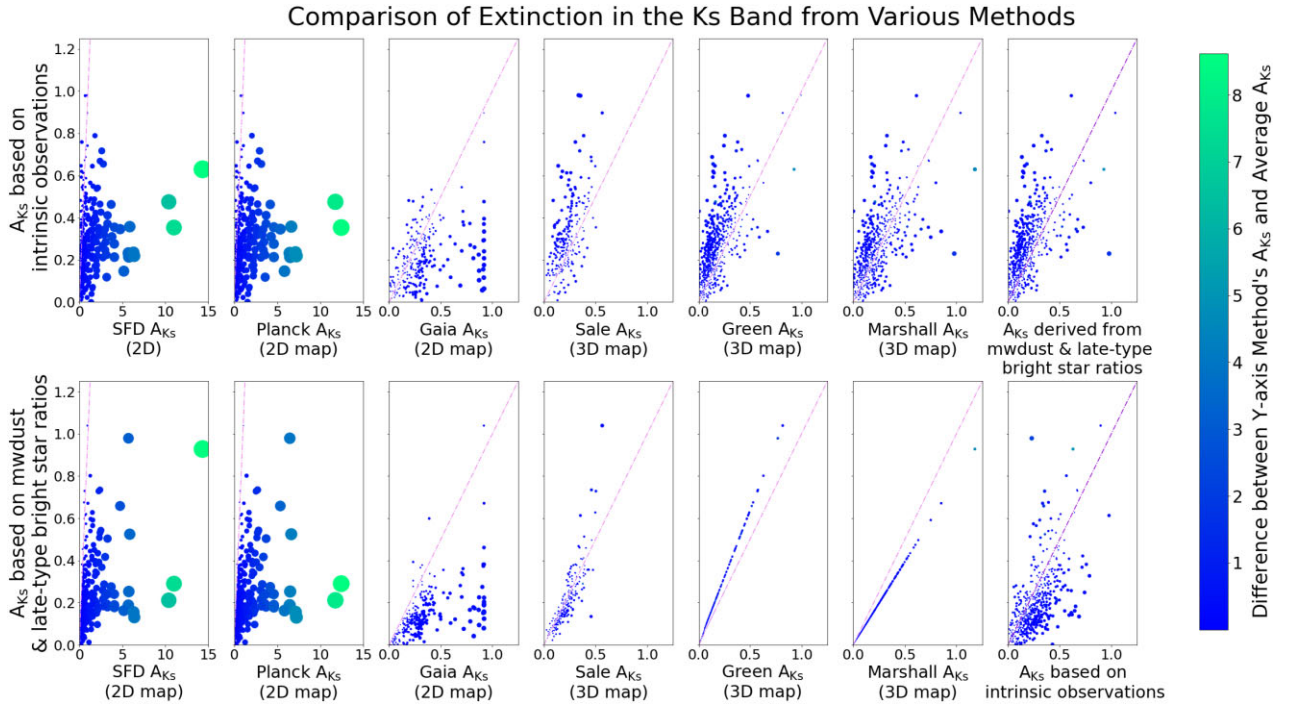

Figure 7. Comparisons of 3D dust maps, MWDUST, and using ICMS to other methods of determining Galactic extinction. The top row shows ICMS along the y-axis and the bottom row shows MWDUST extinction converted to the K_s band along the y-axis, with each being compared to 2D maps (Schlafly & Finkbeiner 2011; Planck Collaboration XVI 2014; Delchambre et al. 2022) and 3D maps (Marshall et al. 2006; Sale et al. 2014; Green et al. 2019) along the x-axes. Points are coloured by the size of the difference in the y-axis estimated extinction and the average extinction value across all methods.

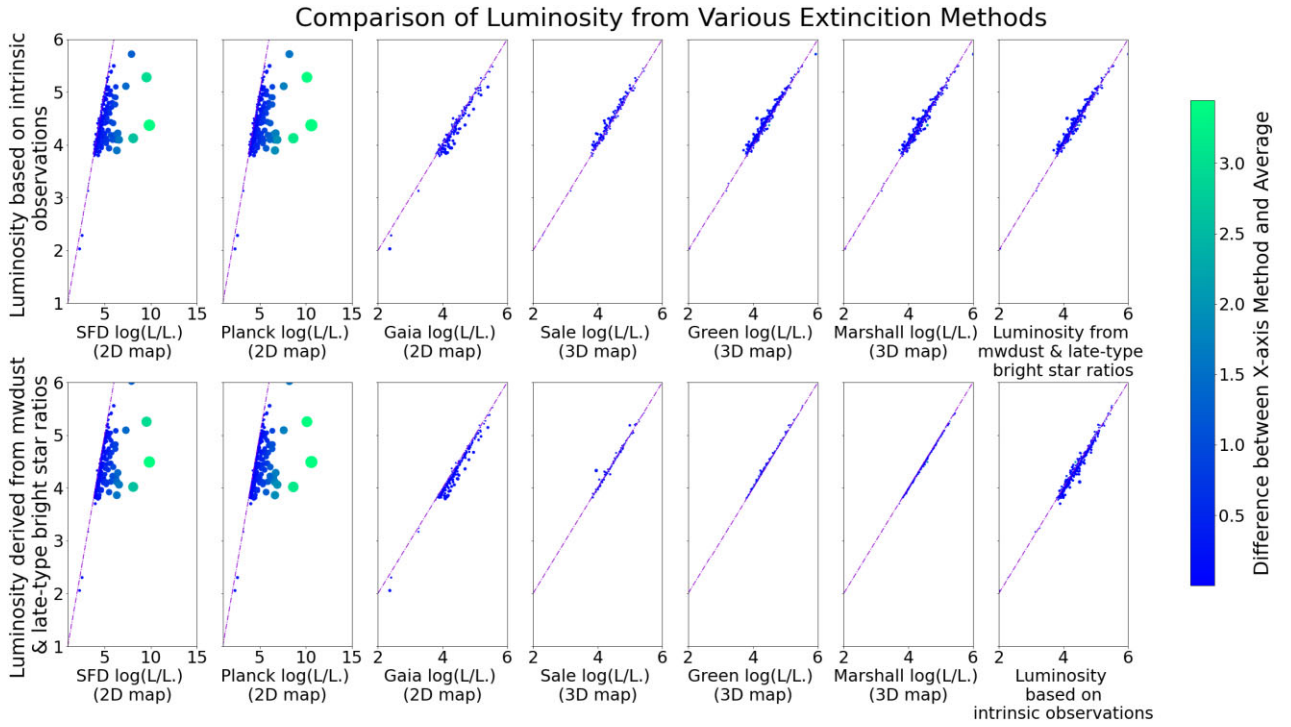

Figure 8. Same as Fig. 7 but showing how different dust correction methods impact our determined luminosity.

Except for the earliest 2D maps of Schlafly & Finkbeiner (2011) and Planck Collaboration XVI (2014), the luminosities determined by our dust method remain very similar to those from more modern dust maps.

We also look into how our final estimates for bolometric luminosity compare to those in the literature; their values are more confident as they generally focus on a small sample of RSG candidates and directly determine their characteristics. Using our reference RSGs

from Section 2.1.2, we compare the changes that would result from using DR2 geometric distance (`r_est`; Bailer-Jones et al. 2018) instead of DR3's. The mean, median, and mode values for the difference between the reference RSG values and those estimated using our method and DR3 are all ≥ 15 per cent smaller than those from DR2. The general trend of DR3 based values being closer to their reference values reinforces our use of distances primarily from `r_geo_med` but supplemented with `r_est`. However, both methods systematically underestimate luminosity, with a few outliers generally caused by areas of high dust. Stars which have the required luminosity and $T_{\rm eff}$ are very likely to be bright or brighter than our limits as systematics taken into account would shift them higher, validating the inclusion of stars whose estimated values are not high enough but whose uncertainty places them in one of the two retained regions.

5 COMPARISON WITH PREVIOUS WORKS

Collecting the Milky Way's RSGs has been a necessary challenge, particularly for two areas of astrophysics: stellar astronomy and studies of massive stars pre-explosion (Messineo & Brown 2019; Messineo 2023) and astroparticle focused more on neutrinos and the explosion itself (Nakamura et al. 2016; Mukhopadhyay et al. 2020). The motivations and approaches behind all efforts vary considerably.

Messineo & Brown (2019) focused on finding candidate RSGs in *Gaia* DR2. They compiled Galactic spectral catalogues whose objects are in *Gaia* DR2 to estimate the effective temperature ($T_{\rm eff}$) and determine reliable distance measurements, and match them with infrared and optical measurements from various sources. Their combination of multiple bands with effective temperature allowed them to estimate stellar bolometric magnitude in two ways: by using photometric measurements and by integrating under the SED. This resulted in 889 late-type stars and 43 highly probable RSGs.

The release of *Gaia* DR3 and associated data products presented new opportunities to categorize Galactic RSGs. A new list of late-type bright stars, including RSG and bright AGBs was developed using *Gaia* DR3 Apsis (Bailer-Jones et al. 2013; Delchambre et al. 2022) and *Gaia* DR3 GSP-Phot and GSP-Spec parameters of known K- and M-type stars of Class I luminosity by Messineo (2023). In addition to the previous work, there are 203 new entries of late-type bright stars with 15 S-type, 1 S/C, 9 C-rich, and 20 confirmed new RSGs with six having bolometric magnitudes brighter than the AGB limit.

For both Nakamura et al. (2016) and Mukhopadhyay et al. (2020), potential progenitors and their properties were compiled from the literature. Nakamura et al. (2016) explored the multimessenger signals of a nearby CCSN, and simulated a complete sequence of signals, detectors' abilities limited their sample to ∼3 kpc. For future detection prospects, Nakamura et al. (2016) compiled 212 Wolf-Rayet stars along with RSG candidates, sometimes with the luminosity class of II or even III. Mukhopadhyay et al. (2020) heavily focused on the potential of liquid scintillators neutrino detectors to localize pre-supernova neutrino signals, a task which may be achieved at close distances. Thus, their list is restricted to $\lesssim 1$ kpc, for a total of 31 containing red and blue massive stars. No analysis is done beyond compilation to determine the accuracy of CCSN progenitor status. As the purpose and method for listing possible CCSN progenitors candidates were relatively consistent, there was an overlap of the most nearby candidates.

By comparison, our work resulted in 578 Milky Way candidate RSGs. To obtain this enhancement, we begin by following the method of Messineo & Brown (2019) but modify it in a few key ways to tailor our analysis for use with multimessenger astronomy. For example, we do not restrict our sample to those in the Galactic plane, and we place an emphasis on having more RSGs at the expense of having slightly more AGB stars contaminating our list, similar to Nakamura et al. (2016) and Mukhopadhyay et al. (2020) but to a lesser degree. Furthermore, we work with the updated *Gaia* DR3, though we do not yet include *Gaia* DR3 spectra or Apsis parameters as Messineo (2023) does. Our method for determining a single spectral type for objects with multiple designations considers the increase in data and follows a more strict prescription than that of Messineo & Brown (2019). We also implement a new method that adds 33 unique highly probable and likely RSGs. This method uses a sample of known K- and M-type stars included in *Gaia* DR3 to determine a *Gaia G* band photometry cut-off. It is combined with external spectra, working similarly to Messineo (2023)'s use of Gaia Apsis parameters and spectra.

Even though we obtain a larger number of RSG candidates – with potentially more contaminants – it is worth pointing our we are far from complete. Given the Milky Way's core-collapse supernova rate of a few per century (Tammann, Loeffler & Schroeder 1994; Rozwadowska, Vissani & Cappellaro 2021) and the duration of the RSG phase for the most common $8M_{\odot}$ star being ∼0.5 Myr (Eldridge, Izzard & Tout 2008), the number of RSGs at any given time in the Milky Way is approximately $\sim 5 \times 10^5/100 \sim 5000$ (Gehrz 1989).

6 MULTIMESSENGER ASTRONOMY

Multimessenger astronomy is based on coordinating observations across multiple messengers – from electromagnetic radiation to gravitational waves and neutrinos – and on the interpretation of the joint results to optimize the science attained. With coordinated efforts, both detections and non-detections lead to useful information on the physics behind different astrophysical phenomena. A key to successful coordination for transient events such as CCSNe is in aligning the observatories in time. To this end, advanced warning of an impending CCSN is highly useful.

Neutrinos will be prolifically produced during stellar CC, and since they arrive minutes to days before the rise of the electromagnetic emission, provide the desired early alert (see e.g. Kharusi et al. 2021). Also, neutrino production rapidly rises during the last stages of nuclear burning, which can provide an advanced warning of the CC itself. One early established neutrino alert system is the SN Early Warning System (Antonioli et al. 2004). SNEWS provides an early warning for a Galactic CCSN by tracking coincidences between neutrino experiments. In addition to providing coincident alerts, the successor to SNEWS, SNEWS 2.0, will aim at providing as much useful information as possible to capture the multimessenger counterparts of the CC (Kharusi et al. 2021). In particular, the distance and position of the source will be key parameters that can be estimated with the neutrino data. The `snewpdag`[5] software will be in charge of these calculations and used to release automated information in case of a CCSN alert.

SNEWS also coordinates with citizen astronomers, for instance, with the American Association of Variable Star Observers (AAVSO) to monitor potential CCSNe candidates long before they collapse, allowing more detailed observations on the development of stars as they evolve towards CC. The alert follow-up is being facilitated with the Recommender Engine For Intelligent Transient Tracking (Sravan et al. 2020). This is particularly useful as peculiar behaviour

[5] https://github.com/SNEWS2/snewpdag

prior to CC has been documented in several SNe with spurious observations. For example, the progenitor of SN 2009ip underwent a series of mini explosions prior to SN (Smith et al. 2022). It could also allow us to check for evidence of pre-SN mass-loss, more accurately relate explosion energy with progenitors' initial mass, and define the relationship of light-curve plateau brightness, temperature evolution of SN emission, and progenitor radius.

6.1 Directional information from neutrinos

There are two main methods to obtain angular pointing information with the neutrino data: a direct direction reconstruction using anisotropic interactions and triangulation. The first exploits an interaction between the neutrino and a target with some intrinsic directionality with a detector that can exploit such information. For example, the electron scatters preferentially along the neutrino direction in neutrino-electron elastic scattering. Cherenkov detectors can track the direction through the light that is released when the electron is kicked. With this method, Super-Kamiokande can give the direction within 3–8 degrees for an SN at 10 kpc (Mukhopadhyay et al. 2020). In relation to our catalogue, neutrino pointing can reduce the possible potential stellar candidates on average within the error circles of 3–8 degrees down to 12–41 stars, respectively. Other neutrino interactions either do not retain very well directional information or have smaller cross sections.

The second method is triangulation (or, more precisely, multi-lateration), which uses the relative arrival times of the neutrino burst through multiple detectors in different geographical locations to determine from where those neutrinos originate (Beacom & Vogel 1999; Vogel 1999; Mühlbeier, Nunokawa & Zukanovich Funchal 2013). The time of flight through the Earth for a neutrino is on the order of milliseconds. The success of the triangulation approach, therefore, depends on detectors registering samples of neutrino events large enough to achieve sufficient burst timing precision, or to have a very low background so as to precisely tell which is the first signal event. It also benefits from wide geographical spread among the contributing detectors. Estimates for the precision of triangulation under various assumptions and as a function of distance and location have been studied in various forms (e.g. Linzer & Scholberg 2019; Coleiro et al. 2020; Hansen, Lindner & Scholer 2020; Kato, Ishidoshiro & Yoshida 2020) where the most favourable conditions give a 1σ area of a few per cent of the sky.

Once a trigger is received, SNEWS's network runs the information through a pointing algorithm, producing a trigger packet of a skymap of direction probabilities and distance estimations (See Section 6.2). Direction information from anisotropic interactions, calculated by individual experiments, can be incorporated into a final probability skymap, which can then be used to prioritize follow-up observation, especially if one is able to focus on a finite list of high-probability candidates, maximizing the prospects of obtaining both pre-SN observations and capturing the early rise of the SN with better sensitivity and cadence.

In Fig. 9, we show simulations of the triangulation error box estimated with the SNEWPDAG package and overlaid with our RSG list. We considered four stars ([W60] C10, X-46, CD-34 11794, and HD 303250) in the catalogue covering different positions on the sky, distances, and stellar clustering. We fix the CC time epoch to illustrate both sky location dependence and the distance dependence. Simulations using SNEWPY (Baxter et al. 2022) of the CCSN models in Burrows & Vartanyan (2021), with the corresponding stellar masses, have been used for this study. We apply the method described in Coleiro et al. (2020) to inverse beta decay ($\overline{\nu}_e p \rightarrow e^+ n$) samples at four detectors (Super-Kamiokande, JUNO, IceCube, and SNO +) to estimate the time delays. This method to estimate the time delay uncertainties by combining the observed neutrino light curves was chosen as it does not rely on any model template. The time uncertainties obtained range from 1 ms, for distances up to ∼1 kpc, to ∼10 ms for 12–13 kpc. We see that in all cases, the angular resolution significantly reduces the number of possible candidates, and further reduction can be achieved with the use of a distance estimate.

6.2 Distance estimate with neutrinos

It was shown in Segerlund, O'Sullivan & O'Connor (2021) that the $\overline{\nu}_e$ event rate in the early stages of the neutrino burst is related to the CCSN distance. Two methods proposed have been implemented into SNEWPDAG: the first compares the observed number of events (n_{50}) to the expected value weighted over the initial mass function (the 'IMF method'), and the second (the 'f_Δ method') relies on a distance independent parameter, f_Δ = N(50)/N(100–150), and its linear relation with n_{50} (Horiuchi et al. 2017). Here, N(50)/N(100–150) is the ratio of the expected number of events in the two respective time windows. We use both approaches to evaluate the distance uncertainty for our selected four candidate stars of the catalogue, using a detector of the size of Super-Kamiokande or JUNO. We consider the same CCSN models as in Section 6.1 and include the systematic uncertainty due to the model dependence of the methods. A further systematic uncertainty arises from the time uncertainty of Section 6.1, which affects how the time windows (and therefore their event counts) are reckoned. This systematic effect has been studied by shifting the neutrino light curve in simulations with respect to the true bounce time according to the expected time uncertainty. The results, shown in Fig. 10, show the complementarity between the two methods: the f_Δ method, dominated by statistical uncertainty, works better at smaller distances, while the IMF method outperforms at larger distances, albeit dominated by systematic uncertainties. Using this information on top of the triangulation skymap, the number of RSGs is further reduced in the best of cases to a few stars. For areas of high stellar density, the reduction is to less than 33 per cent of the candidates falling within the 90 per cent confidence level sky region, as seen in Fig. 9.

6.3 Implications for MMA

Obtaining detailed observations of a CCSN, from pre-explosion and neutrino burst through to shock breakout and the SN, would provide a treasure trove of data. Our RSG list would help realize this in the next Galactic CCSN by providing likely targets in the event of a neutrino alert in the future.

To date, pre-explosion observations of CCSN have been few and far between, but they have revealed interesting, unexpected behaviours. For example, the progenitor of SN2009ip underwent a series of mini explosions prior to SN (Maza et al. 2009; Miller et al. 2009; Smith et al. 2010) and SN1987a had a blue supergiant progenitor (Sonneborn, Altner & Kirshner 1987) contrary to the standard expectation for an RSG progenitor. Pre-explosion images have also revealed the so-called 'red supergiant problem' wherein Type IIP SN progenitors appear to have a maximum mass of $\sim 17 M_\odot$, which is smaller than the most massive RSGs seen locally (Smartt et al. 2009). Various possible solutions have been suggested. For example, the most massive RSGs may not be exploding as Type IIP SNe, necessitating a revision of our understanding of how RSGs end their lives, with deep implications for the formation rate of black holes and

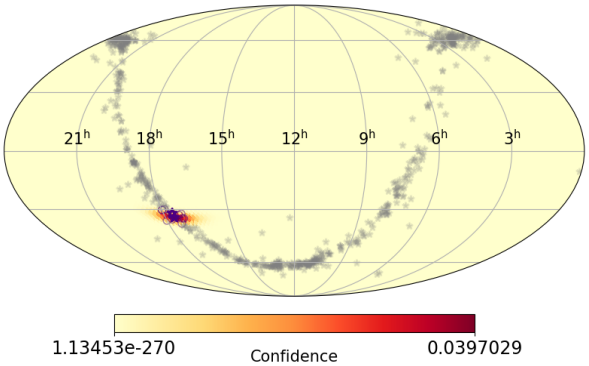

(a) Calculations based on CD-34 11794 (263°, -34°, and 4.1 kpc) as the progenitor. 15 stars lie within the 90% credible region with 2 of those matching the combined distance estimation and angular resolution.

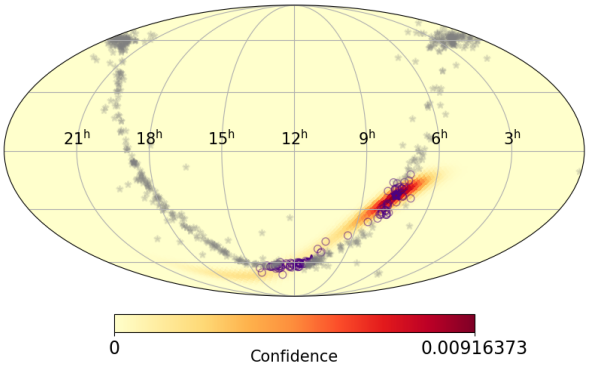

(c) Calculations based on X-46 (113°, -22° and 7.6 kpc) as the progenitor. 105 stars lie within the 90% credible region, with 2 matching the combined distance estimation and angular resolution.

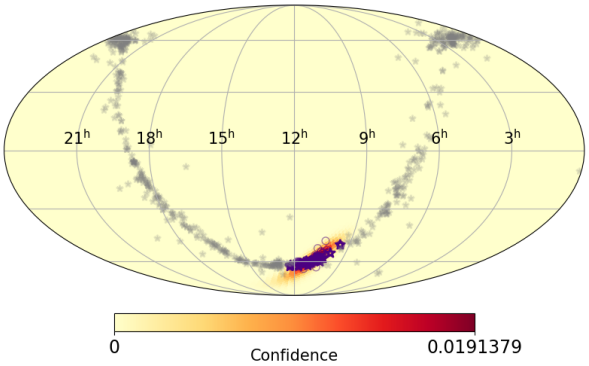

(b) Calculations based on HD 303250 (161°, -58°, and 2.4 kpc) which lies within cluster CAR OB1 as the progenitor. 85 stars lie within the 90% credible region, with 20 of those matching the combined distance estimation and angular resolution.

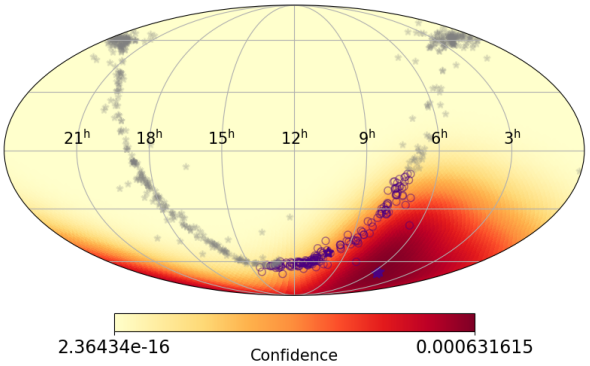

(d) Calculations based on [W60] C10 (83°, -67°, 12.9 kpc) as the progenitor. 187 stars lie within the 90% credible region, with 3 of those matching the combined distance estimation and angular resolution.

Figure 9. Confidence level localization skymaps derived from triangulation, using the simulation of four CCSN events corresponding to the four stars shown in Fig. 10. Overlaid is our RSG list (light grey stars), with those inside the 90 per cent angular error as dark purple open circles. RSGs, which also match the distance estimated from neutrinos, are shown by dark purple stars. The four panels show different sources at various RA, Dec, and distances.

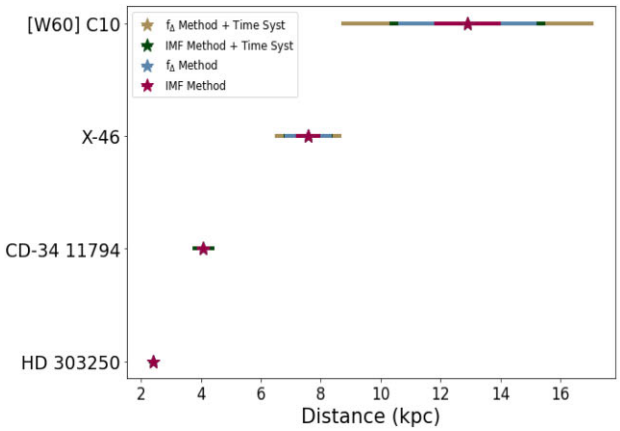

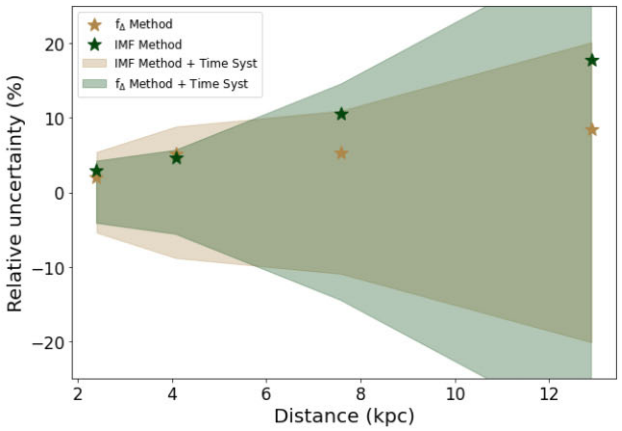

Figure 10. On the right, we see the absolute distance uncertainties in kpc for our four selected stars, and for each of the two distance estimation methods. On the left, the relative distance uncertainty as a function of the distance. Star markers show the method (statistics plus systematics) error for each of the stars. The colour bands correspond to the uncertainties when adding the systematics related to the timing uncertainty.

the influence of SN feedback in galaxy evolution (e.g. Horiuchi et al. 2011; Crain et al. 2015; Kochanek 2015). Alternatively, the discrepancy could derive from our lack of understanding of stellar physics such as mass-loss (Ekström et al. 2012; Georgy 2012), or larger than assumed systematic effects, for example, in bolometric corrections (Davies et al. 2013) or circumstellar extinction (Walmswell & Eldridge 2012; Beasor & Davies 2016a), causing an underestimation of the progenitors mass. Having detailed pre-explosion monitoring

data, in both cadence and multiple bands, would help in all the above debates.

As discussed above, the detection of GWs, multiwavelength photons, and neutrinos provides a unique opportunity to probe the mechanisms of CC; however, the current setup of telescopes and detectors have limitations. Most Galactic SNe should be observable in the optical and virtually all should be observable in the near-IR (Adams et al. 2013). There is even a one-in-three chance for the SN to be visible to the naked eye. Neutrino detections easily cover the entire Milky Way galaxy. The detection by Super-Kamiokande with Gadolinium of a CCSN within 8.5 kpc from the Sun will have a pointing accuracy of ∼3 degrees or better. Note that the region spanning a radius of 8.5 kpc includes 99 per cent of our full catalogue. The detectability of GWs depends strongly on the uncertain core rotation. Nakamura et al. (2016) has shown that for an initially non-rotating core, GW detection is possible for sources up to the Galactic centre if there is a coordinated observation with GW detectors and neutrino telescopes.

Statistically, the most likely distance to the next CCSN is close to the Galactic Centre (Adams et al. 2013). For example, the modelling of the progenitor and Galactic dust as a double-exponential spatial distribution indicates that within 5.8 kpc of the Galactic centre corresponds to 62 per cent of the Galactic CCSNe rate (Adams et al. 2013; Nakamura et al. 2016). While estimates from Galactic distributions of SN remnants (SNR) (Mirizzi, Raffelt & Serpico 2006; Ahlers, Mertsch & Sarkar 2009) show some variation, a radius of ∼6 kpc consistently contains ≥ 50 per cent. In our sample, this results in 41 candidates. On the other hand, CCSN closer to the Sun will have better multimessenger prospects, as we summarized in the previous paragraph. Here, we have 594 stars within 8.5 kpc from the sun (excluding the stars added based on uncertainty), i.e. within the distance regime where neutrinos can provide ∼3 degrees of pointing accuracy and detection prospects for GWs and infrared photons are the most optimistic. Thus, the most promising objects are those within both regions; all 41 stars of the former set are also in the latter. Assuming that only M-type stars are approaching explosion following from the stellar evolutionary paths used in Section 3.2, 36 highly promising stars are retained within the overlapping spatial regions.

Further studies are guaranteed. Within the sample of 36 promising candidates, greater than > 70 per cent have observations in more than three electromagnetic bands. Nevertheless, effort must be made to expand the available high-quality images to more wavelengths and maintain up-to-date follow-up spectra.

7 SUMMARY AND FUTURE WORK

Using two complementary methods, one involving a thorough literature survey and the other using *Gaia* data, we compiled a catalogue of 578 Milky Way RSGs. This is the largest catalogue of its kind in the literature. To differentiate between RSGs and non-RSG contaminants, the most problematically extreme AGBs, we determined the bolometric luminosity and $T_{\rm eff}$. We compared them to stellar evolutionary tracks and galactic AGB surveys. In this context, dust extinction is a major systematic uncertainty, which we estimated using `mwdust`, a 3D dust map, to estimate dust extinction for each star to reduce and prevent correlations in uncertainties. The accuracy of this method was tested by comparing both the estimated extinctions and final luminosities to several alternative methods. Consideration of uncertainties adds another 62 stars that enter the RSG parameter space when individual errors are considered, resulting in a total of 640 candidates.

Along with the information collected to determine their luminosities, the catalogue contains details of each star's known characteristics, including evidence of binary interactions, magnetic fields, variability, and cluster membership. Using the RSG catalogue compiled, we explored the RSG's spatial distribution, stellar radii range, and mass-loss rates. Finally, we explored the impacts of the RSG catalogue for multimessenger observations of the next Galactic CCSN. The intense neutrino burst from the CC of a massive star provides a natural alert, but our RSG catalogue can help suggest locations for observations of a CCSN. Typically, a dozen or so of the RSGs reside within the typical pointing uncertainty given by the neutrino alert.

Future work includes both improvement and expansion of the current catalogue. As extinction is likely our greatest source of error, it seems clear that a better understanding of the complexity of Galactic ISM, including the completion of Galactic 3D dust maps and the excess of CSM around RSGs, such as a more robustly defined $R_{\rm V}$ and associated extinction ratios, would not only improve luminosity estimation but increase the likelihood of including dusty RSGs. Achieving the collection of more candidates in Region C is also important for future work. Issues of AGB contamination could be further mitigated with improvements in infrared spectra and flux values, like those that could be provided by the *Roman Space Telescope* scheduled to launch in 2027. The subsequent infrared CMDs can be combined with knowledge of an object's variability to reduce the ambiguity between AGBs and RSGs. Inspecting the new infrared CMDs can also provide an avenue for finding previously unknown candidates for further study. Expansion of available wavelength and SED fits will allow us to build a more robust profile for each of our candidate RSGs.

While we wait to detect neutrinos, the plan is to improve the characterization of candidates in our list so that post-explosion analysis will require as few assumptions and be as complete as possible. Along with our coordinated efforts to photometric variability monitoring via AAVSO, which is done primarily in the optical band, it would be important to expand the number of pre-explosion images across a greater range of wavelengths for each candidate. Mid-infrared photometry, in particular, will be useful to determine the dusty CSM around the RSGs, for which detailed knowledge of the environment will improve future analyses. This can be accomplished with the *Roman infrared space telescope* and its 2.4-m mirror and Wide Field Instrument. Also important would be starting a campaign of follow-up spectroscopic observations to determine the variability, confirm our estimated luminosities, and collect spectra of the stellar progenitors as close to the explosion as possible. These efforts will also aid in determining fundamental properties like surface gravity and chemical composition to enhance our ability to trace stars from the zero-age main sequence to core collapse.

Some next steps are more immediate; for example, while an RSG is statistically the most likely next CC progenitor, other types of massive stars must also cause CCSNe, such as stripped-envelope SNe. This motivates the inclusion of a broader set of stars to complete further the target list (e.g. Rosslowe & Crowther 2015). Continuation or initiation of monitoring more broadly CC candidates will provide more insight into each.

The next Galactic CCSN will be a once-in-a-generation opportunity to collect exquisite multimessenger observations. With a more complete pre-assembled target list, the completeness of such observations will be improved and would likely shed new insights and potential surprises into stellar and CCSN physics.

ACKNOWLEDGEMENTS

SH is supported by National Science Foundation (NSF) Grant No. PHY-1914409 and No. PHY-2209420. The work of SH is supported by the U.S. Department of Energy Office of Science under award number DE-SC0020262, NSF Grants AST-1908960, PHY-1914409, and PHY-2209420, and JSPS KAKENHI Grant Number JP22K03630 and JP23H0489, and the Julian Schwinger Foundation. This work was supported by World Premier International Research Center Initiative (WPI Initiative), MEXT, Japan.

The work by M. Colomer is supported by the F.R.S.-FNRS (Fonds de la Recherche Scientifique) through the research project IISN 4.4501.17 (40008230). This work is also supported by the National Science Foundation 'Windows on the Universe: the Era of Multi-Messenger Astrophysics' Program: 'WoU-MMA: Collaborative Research: A Next-Generation SuperNova Early Warning System for Multimessenger Astronomy' through Grant Nos. 1914448, 1914409, 1914447, 1914418, 1914410, 1914416, and 1914426.

DM acknowledges NSF support from grants PHY-1914448, PHY-2209451, AST-2037297, and AST-2206532. JT is supported by the Science and Technology Facilities Council (STFC), UK.

We acknowledge with thanks the variable star observations from the AAVSO International Database contributed by observers worldwide and used in this research. We want to give special thanks to George Silvis whose efforts to produce AAVSO TARGETTOOL allow for more efficient monitoring of RSG candidates.

This work has made use of data from the European Space Agency (ESA) mission *Gaia* (https://www.cosmos.esa.int/gaia), processed by the *Gaia* Data Processing and Analysis Consortium (DPAC, https://www.cosmos.esa.int/web/gaia/dpac/consortium). Funding for the DPAC has been provided by national institutions, in particular, the institutions participating in the *Gaia* Multilateral Agreement.

This publication makes use of data products from the Two Micron All Sky Survey, which is a joint project of the University of Massachusetts and the Infrared Processing and Analysis Center/California Institute of Technology, funded by the National Aeronautics and Space Administration and the National Science Foundation.

DATA AVAILABILITY

Data for Table 2 and Appendix A Table A1 is publicly available at https://github.com/SNEWS2/candidate_list.

REFERENCES

Adams S. M., Kochanek C. S., Beacom J. F., Vagins M. R., Stanek K. Z., 2013, ApJ, 778, 164
Ahlers M., Mertsch P., Sarkar S., 2009, Phys. Rev. D, 80, 123017
Alexander M. J., Kobulnicky H. A., Clemens D. P., Jameson K., Pinnick A., Pavel M., 2009, AJ, 137, 4824
Alonso-Santiago J., Negueruela I., Marco A., Tabernero H. M., González-Fernández C., Castro N., 2017, MNRAS, 469, 1330
Andrae R. et al., 2023, A&A, 674, A27
Antonioli P. et al., 2004, New J. Phys., 6, 114
Arnett W. D., Bahcall J. N., Kirshner R. P., Woosley S. E., 1989, ARA&A, 27, 629
Arroyo-Torres B., Wittkowski M., Marcaide J. M., Hauschildt P. H., 2013, A&A, 554, A76
Arroyo-Torres B. et al., 2015, A&A, 575, A50
Asakura K. et al., 2016, ApJ, 818, 91
Astraatmadja T. L., Bailer-Jones C. A. L., 2016, ApJ, 833, 119
Aurière M., Donati J. F., Konstantinova-Antova R., Perrin G., Petit P., Roudier T., 2010, A&A, 516, L2
Avvakumova E. A., Malkov O. Y., Kniazev A. Y., 2013, Astron. Nachr., 334, 860
Bailer-Jones C. A. L., 2015, PASP, 127, 994
Bailer-Jones C. A. L. et al., 2013, A&A, 559, A74
Bailer-Jones C. A. L., Rybizki J., Fouesneau M., Mantelet G., Andrae R., 2018, AJ, 156, 58
Bailer-Jones C. A. L., Rybizki J., Fouesneau M., Demleitner M., Andrae R., 2021, AJ, 161, 147
Baxter A. L. et al., 2022, ApJ, 925, 107
Beacom J. F., Vogel P., 1999, Phys. Rev. D, 60, 033007
Beasor E. R., Davies B., 2016, MNRAS, 463, 1269
Beasor E. R., Davies B., 2017, MNRAS, 475, 55
Beauchamp A., Moffat A. F. J., Drissen L., 1994, ApJS, 93, 187
Bidelman W. P., 1951, ApJ, 113, 304
Bidelman W. P., 1957a, PASP, 69, 147
Bidelman W. P., 1957b, PASP, 69, 326
Blaauw A., 1956a, PASP, 68, 495
Blaauw A., 1956b, ApJ, 123, 408
Blum R. D., Ramírez S. V., Sellgren K., Olsen K., 2003, ApJ, 597, 323
Bonaca A., Conroy C., Wetzel A., Hopkins P. F., Kereš D., 2017, ApJ, 845, 101
Boulon J., 1963, J. Obs., 46, 243
Bovy J., Rix H.-W., Green G. M., Schlafly E. F., Finkbeiner D. P., 2016, ApJ, 818, 130
Bueno A., Gil-Botella I., Rubbia A., 2003, preprint (arXiv:hep-ph/0307222)
Burrows A., Vartanyan D., 2021, Nature, 589, 29
Capuzzo-Dolcetta R., Fragione G., 2015, MNRAS, 454, 2677
Carpenter K. G., Robinson R. D., Harper G. M., Bennett P. D., Brown A., Mullan D. J., 1999, ApJ, 521, 382
Catchpole R. M., Feast M. W., 1981, MNRAS, 197, 385
Charbonneau P., MacGregor K. B., 1995, ApJ, 454, 901
Chieffi A., Limongi M., 2013, ApJ, 764, 21
Clark J. S., Negueruela I., Crowther P. A., Goodwin S. P., 2005, A&A, 434, 949
Clark J. S. et al., 2009, A&A, 498, 109
Coleiro A., Colomer Molla M., Dornic D., Lincetto M., Kulikovskiy V., 2020, Eur. Phys. J. C, 80, 856
Gaia Collaboration, 2023a, A&A, 674, A1
Gaia Collaboration, 2023b, A&A, 674, A37
Comerón F., Figueras F., 2020, A&A, 638, A90
Cox N. L. J. et al., 2012, A&A, 537, A35
Crain R. A. et al., 2015, MNRAS, 450, 1937
Currie T. et al., 2010, ApJS, 186, 191
Dálya G. et al., 2018, MNRAS, 479, 2374
Davies B., Beasor E. R., 2020, MNRAS, 493, 468
Davies B., Figer D. F., Kudritzki R.-P., MacKenty J., Najarro F., Herrero A., 2007, ApJ, 671, 781
Davies B., Figer D. F., Law C. J., Kudritzki R.-P., Najarro F., Herrero A., MacKenty J. W., 2008, ApJ, 676, 1016
Davies B., Origlia L., Kudritzki R.-P., Figer D. F., Rich R. M., Najarro F., Negueruela I., Clark J. S., 2009, ApJ, 696, 2014
Davies B. et al., 2013, ApJ, 767, 3
de Burgos A., Simon-Díaz S., Lennon D. J., Dorda R., Negueruela I., Urbaneja M. A., Patrick L. R., Herrero A., 2020, A&A, 643, A116
Delchambre L. et al., 2023, A&A, 674, A31
Dolan M. M., Mathews G. J., Lam D. D., Lan N. Q., Herczeg G. J., Dearborn D. S. P., 2016, ApJ, 819, 7
Dorda R., Negueruela I., González-Fernández C., Tabernero H. M., 2016a, A&A, 592, A16
Dorda R., González-Fernández C., Negueruela I., 2016b, A&A, 595, A105
Dorda R., Negueruela I., González-Fernández C., 2018, MNRAS, 475, 2003
Drimmel R., Cabrera-Lavers A., López-Corredoira M., 2003, A&A, 409, 205
Drout M. R., Massey P., Meynet G., 2012, ApJ, 750, 97
Ekström S. et al., 2012, A&A, 537, A146
El Eid M. F., The L. S., Meyer B. S., 2009, Space Sci. Rev., 147, 1
Eldridge J. J., Stanway E. R., 2016, MNRAS, 462, 3302
Eldridge J. J., Izzard R. G., Tout C. A., 2008, MNRAS, 384, 1109

Eldridge J. J., Stanway E. R., Xiao L., McClelland L. A. S., Taylor G., Ng M., Greis S. M. L., Bray J. C., 2017, Publ. Astron. Soc. Austr., 34, e058
Elias J. H., Frogel J. A., Humphreys R. M., 1985, ApJS, 57, 91
Eyer L. et al., 2023, A&A, 674, A13
Fawley W. M., Cohen M., 1974, ApJ, 193, 367
Feast M. W., Catchpole R. M., Carter B. S., Roberts G., 1980, MNRAS, 193, 377
Figer D. F., MacKenty J. W., Robberto M., Smith K., Najarro F., Kudritzki R. P., Herrero A., 2006, ApJ, 643, 1166
Flower P. J., 1975, A&A, 41, 391
Flower P. J., 1977, A&A, 54, 31
Förster F. et al., 2018, Nat. Astron., 2, 808
Fragione G., Capuzzo-Dolcetta R., 2016, MNRAS, 458, 2596
Gaia Collaboration, 2016, A&A, 595, A1
Gaia Collaboration, 2018a, A&A, 616, A1
Gaia Collaboration, 2018b, A&A, 616, A10
Gaia Collaboration, 2023, A&A, 674, A34
Garmany C. D., Stencel R. E., 1992, A&AS, 94, 211
Gehrels N., Leventhal M., MacCallum C. J., 1987, ApJ, 322, 215
Gehrz R. D., 1989, in Allamandola L. J., Tielens A. G. G. M., eds, Interstellar Dust. Springer, Dordrecht, the Netherlands, p. 445
Georgy C., 2012, A&A, 538, L8
Gies D. R., Bolton C. T., 1986, ApJS, 61, 419
Ginestet N., Carquillat J. M., Jaschek C., Jaschek M., 1997, A&AS, 123, 135
Ginestet N., Carquillat J. M., Jaschek C., 1999, A&AS, 134, 473
González-Fernández C., Negueruela I., 2012, A&A, 539, A100
González-Fernández C., Dorda R., Negueruela I., Marco A., 2015, A&A, 578, A3
Green G. M. et al., 2015, ApJ, 810, 25
Green G. M., Schlafly E., Zucker C., Speagle J. S., Finkbeiner D., 2019, ApJ, 887, 93
Groenewegen M. A. T., 2022, A&A, 659, A145
Grunhut J. H., Wade G. A., Hanes D. A., Alecian E., 2010, MNRAS, 408, 2290
Guo J. H., Li Y., 2002, ApJ, 565, 559
Gvaramadze V. V., Menten K. M., Kniazev A. Y., Langer N., Mackey J., Kraus A., Meyer D. M.-A., Kamiński T., 2013, MNRAS, 437, 843
Halbwachs J.-L. et al., 2023, A&A, 674, A9
Halliday I., 1955, ApJ, 122, 222
Hansen R. S. L., Lindner M., Scholer O., 2020, Phys. Rev. D, 101, 123018
Harper G. M., Brown A., Lim J., 2001, ApJ, 551, 1073
Harper G. M., Brown A., Guinan E. F., 2008, AJ, 135, 1430
Hartmann L., Avrett E. H., 1984, ApJ, 284, 238
Heger A., Jeannin L., Langer N., Baraffe I., 1997, A&A, 327, 224
Hohle M., Neuhäuser R., Schutz B., 2010, Astron. Nachr., 331, 349
Holl B. et al., 2018, A&A, 618, A30
Horiuchi S., Beacom J. F., 2010, ApJ, 723, 329
Horiuchi S., Beacom J. F., Kochanek C. S., Prieto J. L., Stanek K. Z., Thompson T. A., 2011, ApJ, 738, 154
Horiuchi S., Nakamura K., Takiwaki T., Kotake K., 2017, J. Phys. G, 44, 114001
Humphreys R. M., 1970a, AJ, 75, 602
Humphreys R. W., 1970b, ApJ, 160, 1149
Humphreys R. M., 1978, ApJS, 38, 309
Humphreys R. M., Strecker D. W., Ney E. P., 1972, ApJ, 172, 75
Humphreys R. M., Helmel G., Jones T. J., Gordon M. S., 2020, AJ, 160, 145
Jayasinghe T. et al., 2020, MNRAS, 491, 13
Johnson H. L., 1964, Bol. Obs. Tonantzintla Tacubaya, 3, 305
Johnson H. L., 1966, ARA&A, 4, 193
Joyce M., Leung S.-C., Molnár L., Ireland M., Kobayashi C., Nomoto K., 2020, ApJ, 902, 63
Jura M., Kleinmann S. G., 1990, ApJS, 73, 769
Kato C., Ishidoshiro K., Yoshida T., 2020, Ann. Rev. Nucl. Part. Sci., 70, 121
Keenan P. C., McNeil R. C., 1989, ApJS, 71, 245
Kharusi S. A. et al., 2021, New J. Phys., 23, 031201
Kleinmann S. G., Hall D. N. B., 1986, ApJS, 62, 501
Kochanek C. S., 2015, MNRAS, 446, 1213
Kotake K., 2013, C. R. Phys., 14, 318
Langer N., 2012, ARA&A, 50, 107
Lee T. A., 1970, ApJ, 162, 217
Lenz D., Hensley B. S., Doré O., 2017, ApJ, 846, 38
Leonard P. J. T., Duncan M. J., 1990, AJ, 99, 608
Levesque E. M., 2017, Astrophysics of Red Supergiants, 2514–3433. IOP Publishing, available at:https://dx.doi.org/10.1088/978-0-7503-1329-2
Levesque E. M., 2018, ApJ, 867, 155
Levesque E. M., Massey P., 2020, ApJ, 891, L37
Levesque E. M., Massey P., Olsen K. A. G., Plez B., Josselin E., Maeder A., Meynet G., 2005, ApJ, 628, 973
Levesque E. M., Massey P., Olsen K. A. G., Plez B., Meynet G., Maeder A., 2006, ApJ, 645, 1102
Li W., Wang X., Dyk S. D. V., Cuillandre J.-C., Foley R. J., Filippenko A. V., 2007, ApJ, 661, 1013
Liermann A., Hamann W. R., Oskinova L. M., 2009, A&A, 494, 1137
Lindegren L. et al., 2018, A&A, 616, A2
Lindegren L. et al., 2021, A&A, 649, A4
Linzer N. B., Scholberg K., 2019, Phys. Rev. D, 100, 103005
Lockwood G. W., Wing R. F., 1982, MNRAS, 198, 385
López Ariste A. et al., 2018, A&A, 620, A199
López-Corredoira M., Cabrera-Lavers A., Garzón F., Hammersley P. L., 2002, A&A, 394, 883
Luri X. et al., 2018, A&A, 616, A9
Mackey J., Mohamed S., Neilson H. R., Langer N., Meyer D. M.-A., 2012, ApJ, 751, L10
Maeder A., 2009, Physics, Formation and Evolution of Rotating Stars. Springer, Berlin, Heidelberg
Maíz Apellániz J., Barbá R. H., Fariña C., Sota A., Pantaleoni González M., Holgado G., Negueruela I., Simón-Díaz S., 2021, A&A, 646, A11
Marco A., Negueruela I., 2013, A&A, 552, A92
Marco A., Negueruela I., González-Fernández C., Maíz Apellániz J., Dorda R., Clark J. S., 2014, A&A, 567, A73
Marshall D. J., Robin A. C., Reylé C., Schultheis M., Picaud S., 2006, A&A, 453, 635
Martínez-Palomera J. et al., 2018, AJ, 156, 186
Massey P., 2002, ApJS, 141, 81
Massey P., Evans K. A., 2016, ApJ, 826, 224
Massey P., Olsen K. A. G., 2003, AJ, 126, 2867
Massey P., DeGioia-Eastwood K., Waterhouse E., 2001, AJ, 121, 1050
Massey P., Plez B., Levesque E. M., Olsen K. A. G., Clayton G. C., Josselin E., 2005, ApJ, 634, 1286
Massey P., Olsen K. A. G., Hodge P. W., Strong S. B., Jacoby G. H., Schlingman W., Smith R. C., 2006, AJ, 131, 2478
Massey P., Olsen K. A. G., Hodge P. W., Jacoby G. H., McNeill R. T., Smith R. C., Strong S. B., 2007, AJ, 133, 2393
Massey P., Silva D. R., Levesque E. M., Plez B., Olsen K. A. G., Clayton G. C., Meynet G., Maeder A., 2009, ApJ, 703, 420
Mathias P. et al., 2018, A&A, 615, A116
Mauron N., Josselin E., 2011, A&A, 526, A156
Maza J. et al., 2009, Central Bureau Electronic Telegrams, 1904, 1
McCall M. L., 2004, AJ, 128, 2144
McDonald I., Johnson C. I., Zijlstra A. A., 2011, MNRAS, 416, L6
Medhi B. J., Messina S., Parihar P. S., Pagano I., Muneer S., Duorah K., 2007, A&A, 469, 713
Mengel S., Tacconi-Garman L. E., 2007, A&A, 466, 151
Messineo M., 2023, A&A, 671, A148
Messineo M., Brown A. G. A., 2019, AJ, 158, 20
Messineo M., Habing H. J., Menten K. M., Omont A., Sjouwerman L. O., Bertoldi F., 2005, A&A, 435, 575
Messineo M., Figer D. F., Davies B., Rich R. M., Valenti E., Kudritzki R. P., 2008, ApJ, 683, L155
Messineo M., Zhu Q., Ivanov V. D., Figer D. F., Davies B., Menten K. M., Kudritzki R. P., Chen C. H. R., 2014, A&A, 571, A43
Messineo M., Zhu Q., Menten K. M., Ivanov V. D., Figer D. F., Kudritzki R.-P., Chen C. H. R., 2016, ApJ, 822, L5
Messineo M., Zhu Q., Menten K. M., Ivanov V. D., Figer D. F., Kudritzki R.-P., Chen C. H. R., 2017, ApJ, 836, 65
Milam S. N., Woolf N. J., Ziurys L. M., 2009, ApJ, 690, 837

Miller A. A., Li W., Nugent P. E., Bloom J. S., Filippenko A. V., Merritt A. T., 2009, Astron. Telegram, 2183, 1
Mirizzi A., Raffelt G. G., Serpico P. D., 2006, J. Cosmol. Astropart. Phys., 2006, 012
Moravveji E., Guinan E. F., Khosroshahi H., Wasatonic R., 2013, AJ, 146, 148
Morgan W. W., Keenan P. C., Kellman E., 1943, An Atlas of Stellar Spectra, with an Outline of Spectral Classification. University of Chicago, Chicago
Mühlbeier T., Nunokawa H., Zukanovich Funchal R., 2013, Phys. Rev. D, 88, 085010
Mukhopadhyay M., Lunardini C., Timmes F. X., Zuber K., 2020, ApJ, 899, 153
N. Houk, Swift C., 1999, Michigan Spectral Survey, Ann Arbor, Dep. Astron., Univ. Michigan, 5, 0
Nakamura K., Horiuchi S., Tanaka M., Hayama K., Takiwaki T., Kotake K., 2016, MNRAS, 461, 3296
Negueruela I., González-Fernández C., Marco A., Clark J. S., Martínez-Núñez S., 2010, A&A, 513, A74
Negueruela I., González-Fernández C., Marco A., Clark J. S., 2011, A&A, 528, A59
Negueruela I., Marco A., González-Fernández C., Jiménez-Esteban F., Clark J. S., Garcia M., Solano E., 2012, A&A, 547, A15
Neugent K. F., Massey P., Skiff B., Meynet G., 2012, ApJ, 749, 177
Neugent K. F., Levesque E. M., Massey P., Morrell N. I., 2019, ApJ, 875, 124
Neugent K. F., Massey P., Georgy C., Drout M. R., Mommert M., Levesque E. M., Meynet G., Ekström S., 2020, ApJ, 889, 44
Noriega-Crespo A., van Buren D., Cao Y., Dgani R., 1997, AJ, 114, 837
Odrzywolek A., Misiaszek M., Kutschera M., 2004, Astropart. Phys., 21, 303
Ott C. D., 2009, Class. Quantum Gravity, 26, 063001
Pantaleoni González M., Maíz Apellániz J., Barbá R. H., Negueruela I., 2020, Res. Notes Am. Astron. Soc., 4, 12
Pecaut M. J., Mamajek E. E., Bubar E. J., 2012, ApJ, 746, 154
Pesch P., 1967, ApJ, 147, 381
Pierce M. J., Jurcevic J. S., Crabtree D., 2000, MNRAS, 313, 271
Planck Collaboration XVI, 2014, A&A, 571, A11
Poelarends A. J. T., Herwig F., Langer N., Heger A., 2008, ApJ, 675, 614
Rayner J. T., Cushing M. C., Vacca W. D., 2009, ApJS, 185, 289
Ren Y., Jiang B.-W., Yang M., Gao J., 2019, ApJS, 241, 35
Ren Y., Jiang B., Yang M., Wang T., Jian M., Ren T., 2021, ApJ, 907, 18
Rosslowe C. K., Crowther P. A., 2015, MNRAS, 447, 2322
Rozwadowska K., Vissani F., Cappellaro E., 2021, New Astron., 83, 101498
Sale S. E. et al., 2014, MNRAS, 443, 2907
Schlafly E. F., Finkbeiner D. P., 2011, ApJ, 737, 103
Schlegel D. J., Finkbeiner D. P., Davis M., 1998, ApJ, 500, 525
Scholberg K., 2012, Annu. Rev. Nucl. Part. Sci., 62, 81
Segerlund M., O'Sullivan E., O'Connor E., 2021, preprint (arXiv:2101.10624)
Shappee B. J. et al., 2014, ApJ, 788, 48
Shinnaga H., Claussen M. J., Yamamoto S., Shimojo M., 2017, PASJ, 69, L10
Siess L., 2006, A&A, 448, 717
Skiff B. A., 2014, VizieR Online Data Catalog, p. B/mk
Skrutskie M. F. et al., 2006, AJ, 131, 1163
Smartt S. J., 2015, Publ. Astron. Soc. Austr., 32, e016
Smartt S. J., Maund J. R., Hendry M. A., Tout C. A., Gilmore G. F., Mattila S., Benn C. R., 2004, Science, 303, 499
Smartt S. J., Eldridge J. J., Crockett R. M., Maund J. R., 2009, MNRAS, 395, 1409
Smith N. et al., 2010, AJ, 139, 1451
Smith N., Andrews J. E., Filippenko A. V., Fox O. D., Mauerhan J. C., Van Dyk S. D., 2022, MNRAS, 515, 71
Sonneborn G., Altner B., Kirshner R. P., 1987, ApJ, 323, L35
Sravan N., Milisavljevic D., Reynolds J. M., Lentner G., Linvill M., 2020, ApJ, 893, 127
Stock S., Reffert S., Quirrenbach A., 2018, A&A, 616, A33
Stothers R., 1969, ApJ, 156, 541
Stothers R., 1972, A&A, 18, 325
Tabernero H. M., Dorda R., Negueruela I., Marfil E., 2021, A&A, 646, A98
Tammann G. A., Loeffler W., Schroeder A., 1994, ApJS, 92, 487
Taniguchi D., Winered Team, 2021, in The 20.5th Cambridge Workshop on Cool Stars, Stellar Systems, and the Sun (CS20.5). p. 185
Taniguchi D. et al., 2021, MNRAS, 502, 4210
Tessore B., Lèbre A., Morin J., Mathias P., Josselin E., Aurière M., 2017, A&A, 603, A129
Tetzlaff N., Neuhäuser R., Hohle M. M., 2011, MNRAS, 410, 190
Tomàs R., Semikoz D., Raffelt G. G., Kachelrieß M., Dighe A. S., 2003, Phys. Rev. D, 68, 093013
Tominaga N., Morokuma T., Blinnikov S. I., Baklanov P., Sorokina E. I., Nomoto K., 2011, ApJS, 193, 20
Townes C. H., Wishnow E. H., Hale D. D. S., Walp B., 2009, ApJ, 697, L127
Tremko J., Bakos G. A., Žižňovský J., Pribulla T., 2010, Contrib. Astron. Obs. Skaln. Pleso, 40, 83
Van Belle G. T., Creech-Eakman M. J., Hart A., 2009, MNRAS, 394, 1925
Van Dyk S. D., 2017, Phil. Trans. R. Soc. A: Math. Phys. Eng. Sci., 375, 20160277
Van Dyk S. D. et al., 2012, AJ, 143, 19
van Dyk S. D., Filippenko A. V., Fox O. D., Kelly P. L., Milisavljevic D., Smith N., 2017, Astron. Telegram, 10378, 1
van Leeuwen F., 2007, A&A, 474, 653
van Loon J. T., Cioni M. R. L., Zijlstra A. A., Loup C., 2005, A&A, 438, 273
Verhoelst T., van der Zypen N., Hony S., Decin L., Cami J., Eriksson K., 2009, A&A, 498, 127
Vidotto A. A., Jatenco-Pereira V., 2006, ApJ, 639, 416
Vlemmings W. H. T., Diamond P. J., van Langevelde H. J., 2002, A&A, 394, 589
Vlemmings W. H. T., van Langevelde H. J., Diamond P. J., 2005, A&A, 434, 1029
Vogel P., 1999, preprint (arXiv:astro-ph/9904338)
Walmswell J. J., Eldridge J. J., 2012, MNRAS, 419, 2054
Westerlund B. E., 1987, A&AS, 70, 311
White D. J., Daw E. J., Dhillon V. S., 2011, Class. Quantum Gravity, 28, 085016
White N. M., Wing R. F., 1978, ApJ, 222, 209
Wittkowski M., Hauschildt P. H., Arroyo-Torres B., Marcaide J. M., 2012, A&A, 540, L12
Wittkowski M., Arroyo-Torres B., Marcaide J. M., Abellan F. J., Chiavassa A., Guirado J. C., 2017, A&A, 597, A9
Wood P. R., Bessell M. S., Fox M. W., 1983, ApJ, 272, 99
Yang M., Jiang B. W., 2011, ApJ, 727, 53
Yang M., Jiang B. W., 2012, ApJ, 754, 35
Yang M. et al., 2019, A&A, 629, A91
Yang M. et al., 2021, A&A, 646, A141
Yaron O. et al., 2017, Nat. Phys., 13, 510
Zinn R., 1985, ApJ, 293, 424

APPENDIX A: SAMPLE CHARACTERISTICS

Table A1 lists 44 stars of our final sample, showing select columns. The full table is available in machine-readable form on Vizier and at https://github.com/SNEWS2/candidaten_list. The columns of the full table are:

Column (1): Alias
Column (2): *Gaia* DR3 source id
Column (3): *Gaia* DR2 source id
Column (4): Adopted mean spectral type
Column (5): Spectral type(s)
Column (6): Spectral type references (format is only the last name of first author and year)
Columns (7)–(8): Either the same as reference if the spectral type was derived in that reference or the source cited for the spectral type given in the reference and associated number used in tables
Columns (9)–(10): Effective temperature and associated errors based on spectral types

Table A1. Summary of calculated parameters for the highly probable and probable Galactic RSGs derived from either the Compilation-based or *Gaia*-based Method. Flags showing if an object has been identified as a Binary or Variable star are shown, but the full details are included in the unabridged catalogue. The full table is publicly available at https://github.com/SNEWS2/candidate_list.

Alias	SpType_a	$\log(\frac{L}{L_\odot})$	$\log(\frac{R}{R_\odot})$	$\log(\dot{M})$ $\log(M_\odot yr^{-1})$	Binary_Flag	Binary_Ref_#[1]	Variable_Flag	Variable_Ref_#[1]	Cluster/ Association
V∗ V348 Vel	M2	5.1	2.9	−4.5	–	–	Variable	II, I, IV, III	–
HD 237025	M2	4.6	2.7	−4.9	Binary	III, IV	Variable	IV, III	Perseus Arm
2MASS J18412383-0526073	M0	4.2	2.4	−5.6	–	–	Variable	III	Stephenson 2
[O66] 8:1003	K5	3.2	1.9	−6.6	–	–	–	–	–
UCAC2 5411346	M1	3.9	2.3	−5.8	–	–	Variable	IV, III	–
V∗ V778 Cas	M2	4.4	2.6	−5.2	–	–	Variable	II, IV, III	PER OB1
V∗ V466 Cas	M1.5	4.4	2.6	−5.2	–	–	Variable	IV, III	NGC 457
2MASS J19192791+1453516	M1.5	3.9	2.3	−5.8	Binary	III	Variable	IV, III	–
V∗ V441 Per	M2	4.7	2.7	−4.9	–	–	Variable	II, IV, III	PER OB1
IRC+60091	M2	4.7	2.7	−4.9	–	–	Variable	II, I, IV, III	PER OB1
CD-61 3575	M2	4.9	2.9	−4.6	Binary	V, 0	Variable	II, IV, III	–
IRAS 18104–1755	K2	3.8	2.2	−6.1	–	–	Variable	II, IV, III	Cluster near Hess J1813-178
BD+60 299	M2	4.9	2.9	−4.6	–	–	Variable	II, I, IV, III	Perseus Arm
DO 42086	M4	4.8	2.8	−4.7	Binary	III	Variable	II, I, IV, III	Perseus Arm
IRAS 22096+5619	M2	4.4	2.6	−5.3	Binary	III	Variable	III	Perseus Arm
IRAS 01046+6309	K3	4.3	2.4	−5.6	–	–	–	–	Perseus Arm
V∗ AS Cep	M3	4.9	2.9	−4.6	–	–	Variable	II, I, IV, III	–
DO 24315	M3	4.4	2.6	−5.2	Binary	II	Variable	II, I, IV, III	Perseus Arm
HD 174797	M2.5	4.1	2.4	−5.5	–	–	Variable	II, IV, III	–
HD 101779	M0	3.9	2.3	−5.8	–	–	Variable	IV, III	–
[2018MZM] 92	K5.5	4.2	2.4	−5.6	–	–	Variable	II, I	–
V∗ GS Vel	M2	4.0	2.4	−5.6	–	–	Variable	IV, III	–
HD 89736	M0	4.0	2.3	−5.8	–	–	Variable	IV, III	–
BM VI 2	M0	4.1	2.4	−5.6	–	–	Variable	IV, III	–
IRC+40427	M1	4.3	2.5	−5.4	–	–	Variable	II, IV	–
IRC−30312	M2.5	5.4	3.1	−4.2	–	–	Variable	II, I	–
UCAC2 09087349	M2.5	4.1	2.4	−5.5	–	–	Variable	IV, III	–
IRAS 22483+5713	K3	4.0	2.3	−5.8	Binary	III	Variable	III	Perseus Arm
V∗ IM Cas	M2	5.0	2.9	−4.6	Binary	III	Variable	II, IV, III	Perseus Arm
HD 45829	K1	3.9	2.2	−6.0	Binary	III	Variable	III	–
BD+10 3764	M3	4.2	2.5	−5.4	Binary	III	Variable	II, IV, III	CAS OB7
[A72c] 37	M0	4.5	2.6	−5.2	–	–	–	–	–
V∗ EH Cas	M3	4.9	2.8	−4.7	Binary	III	Variable	II, IV, III	Perseus Arm
V∗ AZ Cas	K5	4.2	2.5	−5.5	Binary	VI, V, 0,...	Variable	IV, III	CAS OB8
V∗ V605 Cas	M2	4.7	2.8	−4.8	–		Variable	II, IV, III	PER OB1
HD 237006	M1	4.4	2.6	−5.3	Binary	V, 0, 36,...	Variable	IV, III	PER OB1
IRAS 22285+5706	M2	4.2	2.5	−5.4	Binary	III	Variable	IV, III	Perseus Arm
IRAS 00375+6400	M1.5	4.2	2.5	−5.5	Binary	III	Variable	II, III	Perseus Arm
CD-24 13583	M3	4.2	2.5	−5.4	–	–	Variable	IV, III	–
UCAC2 05561199	K7	4.9	2.8	−4.8	–	–	Variable	IV, III	–
BD+62 281	M3	4.7	2.8	−4.8	–	–	Variable	II, IV, III	Perseus Arm
V∗ AV Per	M2	3.8	2.3	−5.8	Binary	III	Variable	II, I, IV, III	CEP OB1
HD 163755	M2	4.3	2.5	−5.3	Binary	III	Variable	IV, III	–

Note. [1] I Holl et al. (2018), II Eyer et al. (2023); Halbwachs et al. (2022); Gaia Collaboration (2023), III AAVSO, IV Shappee et al. (2014); Jayasinghe et al. (2020), V Pantaleoni González et al. (2020), VI Neugent et al. (2019), VII Gvaramadze et al. (2013), VIII Grunhut et al. (2010), IX Tessore et al. (2017). Those denoted by numbers are listed in Table 2.

Columns (11)–(23): Values taken from 2MASS [detailed column descriptions can be found at the link: Cal Tech user guide]

Columns (24)–(58): Values taken from *Gaia* DR3 [detailed column descriptions can be found at the link: Gaia DR3 documentation]

Columns (59)–(61): Values related to *Gaia* EDR3 distance taken from Bailer-Jones et al. (2021)

Columns (62)–(85): Values taken from *Gaia* DR2 [detailed column descriptions can be found at the links: Gaia DR2 documentation and Gaia DR2 RUWE documentation]

Columns (86)–(89): Values related to *Gaia* DR2 distance taken from Bailer-Jones et al. (2018)

Columns (90)–(91): Extinction in the K band and associated error

Column (92): Extinction in the H band

Column (93): Extinction in the J band

Columns (94)–(95): Bolometric correction for K_s band and associated error

Columns (96)–(98): Distance module and associated upper and lower errors

Column (99): Extinction in the V band

Columns (100)–(101): Intrinsic K_s mag and associated error

Column (102): Intrinsic H mag

Column (103): Intrinsic J mag

Columns (104)–(106): Absolute K magnitude and associated upper and lower errors

Columns (107)–(109): Bolometric magnitude and associated upper and lower errors

Column (110): Stellar radius in log form

Column (111): Stellar radius in units of solar radii

Column (112): Log of luminosity in terms of solar luminosity

Column (113): Log of effective temperature

Columns (114)–(116): Galactic coordinates in kiloparsecs

Columns (117): Mass-loss based on equation (6)

Columns (118)–(130): Variable values taken from Gaia DR3 [detailed column descriptions can be found at the link: Gaia DR 3 variable documentation]

Columns (131)–(140): Non-single star values taken from Gaia DR3 [detailed column descriptions can be found at the link: Gaia DR3 non-single star documentation]

Columns (141)–(147): Variable values taken from Gaia DR2 [detailed column descriptions can be found at the link: Gaia DR 2 variable documentation]

Columns (148)–(153): Variable values taken from AAVSO detailed column descriptions can be found at the link: AAVSO VSX Catalog

Columns (154)–(159): Variable values taken from ASAS-SN V detailed column descriptions can be found at the link: ASAS-SN V ariable Star Database

Columns (160)–(163): Variable flag, details on a star's variable status, reference, and each reference's symbol in Table A1

Columns (164)–(167): Binary flag, details on a star's binary status, reference, and each reference's symbol in Table A1

Columns (168)–(170): Measured magnetic field flag, reference, and each reference's symbol in Table A1

Columns (171)–(173): Runaway flag, reference, and each reference's symbol in Table A1

Column (174): Cluster or OB association

Column (175): Method for collection (Compilation-based, *Gaia*-Based, within error bars, or Close star addendum)

Column (176): Simbad Classification

Column (177): Region (A-E)

APPENDIX B: REFERENCES FOR CLOSE STAR TABLE

The references used to create the table detailing all stars whose errors in *Gaia* are too large to retain or are not included, but are generally accepted as RSGs throughout the literature include: Bidelman (1951); Pesch (1967); Lockwood & Wing (1982); Keenan & McNeil (1989); Carpenter et al. (1999); Harper, Brown & Lim (2001); Levesque et al. (2005); Vlemmings et al. (2005); van Leeuwen (2007); Harper, Brown & Guinan (2008); Grunhut et al. (2010); Hohle, Neuhäuser & Schutz (2010); Tremko et al. (2010); Tetzlaff et al. (2011); Cox et al. (2012); Pecaut, Mamajek & Bubar (2012); Wittkowski et al. (2012); Avvakumova, Malkov & Kniazev (2013); Moravveji et al. (2013); Shinnaga et al. (2017); Tessore et al. (2017); López Ariste et al. (2018); Mathias et al. (2018); Stock, Reffert & Quirrenbach (2018); Messineo & Brown (2019); Joyce et al. (2020); Levesque & Massey (2020); Maíz Apellániz et al. (2021); Tabernero et al. (2021); Gaia Collaboration (2023a), and Davies & Beasor (2020).

This paper has been typeset from a TEX/LATEX file prepared by the author.